GEOPHYSICS, VOL. 76, NO. 3 (MAY-JUNE 2011); P. B1–B24, 32 FIGS., 1 TABLE.
10.1190/1.3560016

High-resolution passive seismic tomography (PST) for 3D velocity, Poisson's ratio ν, and P-wave quality Q_P in the Delvina hydrocarbon field, southern Albania

G-Akis Tselentis[1], Nikolaos Martakis[2], Paraskevas Paraskevopoulos[1], and Athanasios Lois[1]

ABSTRACT

We have studied using traveltimes of P- and S-waves and initial seismic-pulse rise-time measurements from natural microearthquakes to derive 3D P-wave velocity V_P information (mostly structural) as well as P- and S-wave velocity V_P/V_S and P-wave quality factor Q_P information (mostly lithologic) in a known hydrocarbon field in southern Albania. During a 12-month monitoring period, 1860 microearthquakes were located at a 50-station seismic network and were used to obtain the above parameters. The data set included earthquakes with magnitudes ranging from –0.1 to 3.0 R (Richter scale) and focal depths typically occurring between 2 and 10 km. Kohonen neural networks were implemented to facilitate the lithological classification of the passive seismic tomography (PST) results. The obtained results, which agreed with data from nearby wells, helped delineate the structure of the reservoir. Two subregions of the investigated area, one corresponding to an oil field and one to a gas field, were correlated with the PST results. This experiment showed that PST is a powerful new geophysical technique for exploring regions that present seismic penetration problems, difficult topographies, and complicated geologies, such as thrust-belt regions. The method is economical and environmentally friendly, and it can be used to investigate very large regions for the optimal design of planned 2D or 3D conventional geophysical surveys.

INTRODUCTION

Passive seismic tomography (PST) has become a well-established technique since its introduction in the mid-1970s. Comprehensive reviews of different aspects of the method are found in Thurber (1986), Kissling (1988), and Iyer and Hirahara (1993). Three-dimensional models of P-wave velocity V_P as well as P- and S-wave velocity V_P/V_S derived from surface passive seismic methodologies have proven useful in investigations of the structure of fault systems and have contributed to our understanding of seismotectonics and seismogenic processes over large areas, particularly in crustal studies (Thurber et al., 1995; Eberhart-Phillips and Michael, 1998; Chiaraba and Amato, 2003).

In the hydrocarbon industry, seismicity has been used mainly as a reservoir monitoring tool for mapping fluid movements (e.g., Rutledge et al., 1998), faults (e.g., Maxwell and Urbancic, 2001), and hydraulic fracturing (e.g., Rutledge and Phillips, 2003). Recently, Zhang et al. (2009) have used the seismicity caused or induced by hydrocarbon production to perform reservoir 3D V_P and V_P/V_S tomography.

PST has also been applied successfully in regional hydrocarbon exploration, demonstrating its potential to map large areas for a relatively low cost compared to conventional 3D seismic surveys (Durham, 2003; Kapotas et al., 2003; Martakis et al., 2003; Martakis et al., 2006). Valoroso et al. (2008) use 4D passive seismic tomography to detect space-time dependency in response to fluid pressure. Tselentis et al. (2006) show that PST can even be applied at a local scale. Although the number of such applications is limited at the moment, with improvements in data acquisition and processing technology, the use of PST as a tool for hydrocarbon exploration and characterization is likely to flourish.

A hydrocarbon reservoir tends to be acoustically softer than regions that are full of an incompressible fluid such as water. Thus, a seismic wave should suffer more attenuation in a hydrocarbon reservoir than in surrounding materials.

One of the geophysical parameters that correlates best with the physical state of the rocks and the percentage of fluid

Manuscript received by the Editor 6 May 2010; revised manuscript received 1 December 2010; published online 00 March 2011.
[1]University of Patras, Seismological Laboratory, Patras, Greece. E-mail: tselenti@upatras.gr; paris@upatras.gr; lois@upatras.gr.
[2]LandTech Enterprises, Athens, Greece. E-mail: nmartakis@landtechsa.com.

J_ID: GPY DOI: 10.1190/1.3560016 Date: 10-March-11 Stage: Page: 2 Total Pages: 24

content is the intrinsic quality factor Q_P of the compressional body waves (Bourbie et al., 1987). As an exploratory tool, attenuation effects have only recently attracted attention (e.g., Hedlin et al., 2001; Tselentis et al., 2010). The Q_P can prove useful in two ways: as a means of correcting seismic data to enhance resolution of conventional imaging techniques and as a direct hydrocarbon or geothermal indicator. The reconstruction of Q_P imaging is considered to be a powerful tool for establishing the distribution of fractured systems characterized by fluid circulation.

The major source of intrinsic attenuation in porous rocks occurs when the motion of the rock and the fluid in the pores uncouple. The rock becomes anelastic as energy is lost because of fluid friction (Pride et al., 2003). If the pore space is completely filled with fluid, the fluid has less mobility than if there is some gas saturation, and attenuation is expected to be higher in a partially fluid-saturated rock (Winkler and Nur, 1982). Theoretically, a subsurface reservoir full of hydrocarbons will tend to be acoustically softer than a porous rock filled only with water (Kumar et al., 2003).

Until recently, most attempts to extract attenuation on a local scale have been restricted to active seismic data recorded at the surface (Evans and Zucca, 1988; Clawson et al., 1989). This approach encounters significant difficulties because the amplitude spectrum of the seismic record contains the imprint of the amplitude spectrum of the earth's reflectivity as well as the amplitude spectrum of the seismic wavelet. In the present investigation, we attempt to extract seismic attenuation values from data obtained from a local high-density microearthquake network.

A method based on the inversion of the rise times is expected to provide the most reliable estimates of intrinsic attenuation (Liu et al., 1994; Tselentis, 1998). In fact, because only a very limited portion of the seismogram is used, the effects of multiple waves generated in thin layers around the recording site are usually minimized (de Lorenzo et al., 2006).

We will always be faced with exploration activity in geologically complex areas such as fold-and-thrust belts. Exploration in these areas is challenging as well as expensive and is driving the oil-exploration industry toward the application of state-of-the-art techniques such as PST.

The rationale for applying PST as a complementary imaging tool has several important advantages. First, tomography is a cost-effective means of imaging a large area with difficult terrain in which conventional seismic exploration is expensive and can be of poor quality because of seismic penetration problems. Second, PST can provide an accurate 3D velocity model that can be used to improve (i.e., migration) existing or lower-quality reflection seismic data. Third, the technique is environmentally friendly, an important consideration in all operational activities. Finally, PST can provide parameters related directly to reservoir properties, such as V_P/V_S and Q_P. These parameters are very difficult to derive from conventional seismic techniques because they require large-amplitude shear waves.

Processing of PST data at a local scale for hydrocarbon exploration is more complicated than applying off-the-shelf 3D inversion algorithms. To get the best resolution of the geologic formations at the lowest cost, we tap an arsenal of techniques, including initial-velocity model selection, simultaneous earthquake hypocenter and 3D velocity models, Q_P inversion, and synthetic and real-data checkerboard tests.

The advantages of applying PST methodologies in the Delvina hydrocarbon region are the easy acquisition of data in a difficult terrain; the low cost in comparison to conventional 2D or 3D methods; and the wave-propagation scheme (the energy traveling directly from hypocenters to the station on the surface), which is not affected by overthrusting, velocity inversions, and problems related to evaporites. The results show that PST can be used to describe known production zones and to identify whether upside potential exists within the study area.

GEOLOGY

The study area is located on the southeastern edge of Albania, close to the border with Greece. This is a key area for various geodynamic models that have been proposed for the Aegean region because the transition of the extensional inner Aegean regime to the compressional outer Aegean occurs in the region. The map of this transition is based on faults that vary from thrust and strike-slip faults to normal faults (King et al., 1983; Underhill, 1989).

The Albanian orogenic belt trends north-northwest–south-southeast and lies between the Dinaric and Hellenic Alps (Figure 1). This belt was established by Alpine orogenic processes in the western Balkans area that were related to the plate convergence between Apulia and Eurasia and the closure of the Mesozoic Tethyan ocean. The Albanian orogenic belt represents a complex orogen made up of a heterogeneous tectonic nappe pile of Paleozoic, Mesozoic, and Cenozoic domains (Aubouin, 1959; Aubouin et al., 1970).

Geotectonically, the study area belongs to the Ionian zone (Robertson and Shallo, 2000), which forms an unbroken, elongated unit (60–70 km long $\times$ 60 km wide) that extends continuously southward into Greece. This unit represents a thin-skinned fold-and-thrust belt with an evaporitic basal décollement, as shown by geophysical and well data (ISPGJ-IGJN, 1982). The outcrop is dominated by large-scale linear folds, forming large anticlines and synclines that are cut by large high-angle reverse faults. A major salt diapir in southern Albania is believed to have protruded upward from underlying thick Triassic salt. Two main tectonic phases are recognized within the Ionian zone: the first occurring in the Middle Miocene and the second occurring around the Miocene–Pliocene boundary. The latter is related to the final thrusting of the Ionian zone southwestward over the Sazani zone (ISPGJ-IGJN, 1983).

SEISMOGRAPH NETWORK AND DATA

A feasibility study is always important before a PST is conducted. This allows the network design to consider a uniform spatial coverage of the area, to use a high sampling resolution, and to take into account the frequency content. In this case, the designed network consisted of 50 three-component 1-Hz LandTech LT100 borehole seismometers and 50 24-bit LandTech LTSR-24 recorders connected to a global positioning system (GPS) unit (Figure 1). The instruments have a flat transfer function for velocity in the 1–100-Hz frequency range. The seismometers were buried in shallow 6-m boreholes to improve the signal-to-noise ratio. Station coordinates were established by differential GPS measurements with a horizontal accuracy of ± 2 m and a vertical accuracy of ± 1 m.

ID: thangabaluP Time: 13:22 I Path: Q:/3b2/GPY#/Vol00000/110059/APPFile/AI-GPY#110059

J_ID: GPY DOI: 10.1190/1.3560016 Date: 10-March-11 Stage: Page: 3 Total Pages: 24

This particular case study covered an area of approximately 1000 km^2 where there is strong attenuation in conventional seismic reflection energy resulting from a high-velocity and/or karstified carbonate outcrop. Recording was conducted continuously for 12 months with a sampling frequency of 100 Hz.

The first stage in the analysis of the seismic data was the automatic search for potential seismic events in the data set of each station. The search was made using the short-term-average/long-term-average (STA/LTA) algorithm tuned for the data set (Lee and Stewart, 1981). Next, the selected events of all stations were automatically cross checked. If an event was detected at more than six stations, it was marked as a real event; otherwise, it was eliminated from the data set. Finally, for each of the seismograms, we manually selected the P- and S-wave phases and measured the corresponding rise times using PASEIS3-LandTech passive seismic processing software. Figure 2 shows an example of a microearthquake recorded at 28 selected stations of the network.

From the acquired data set, more than 2500 events were recorded; 1860 events (Figure 3) were selected for the tomographic inversion, using the criteria described below. The rms error of the hypocentral solution was less than 0.15 s, and horizontal and vertical location errors were less than 1000 m. The events were located within, or very close to, the network area (< 10 km from the outer stations). There were at least six P- and S-wave arrivals per event

The recorded seismicity is presented in map and 3D views in Figure 3. Northwest–southeast and southwest–northeast cross

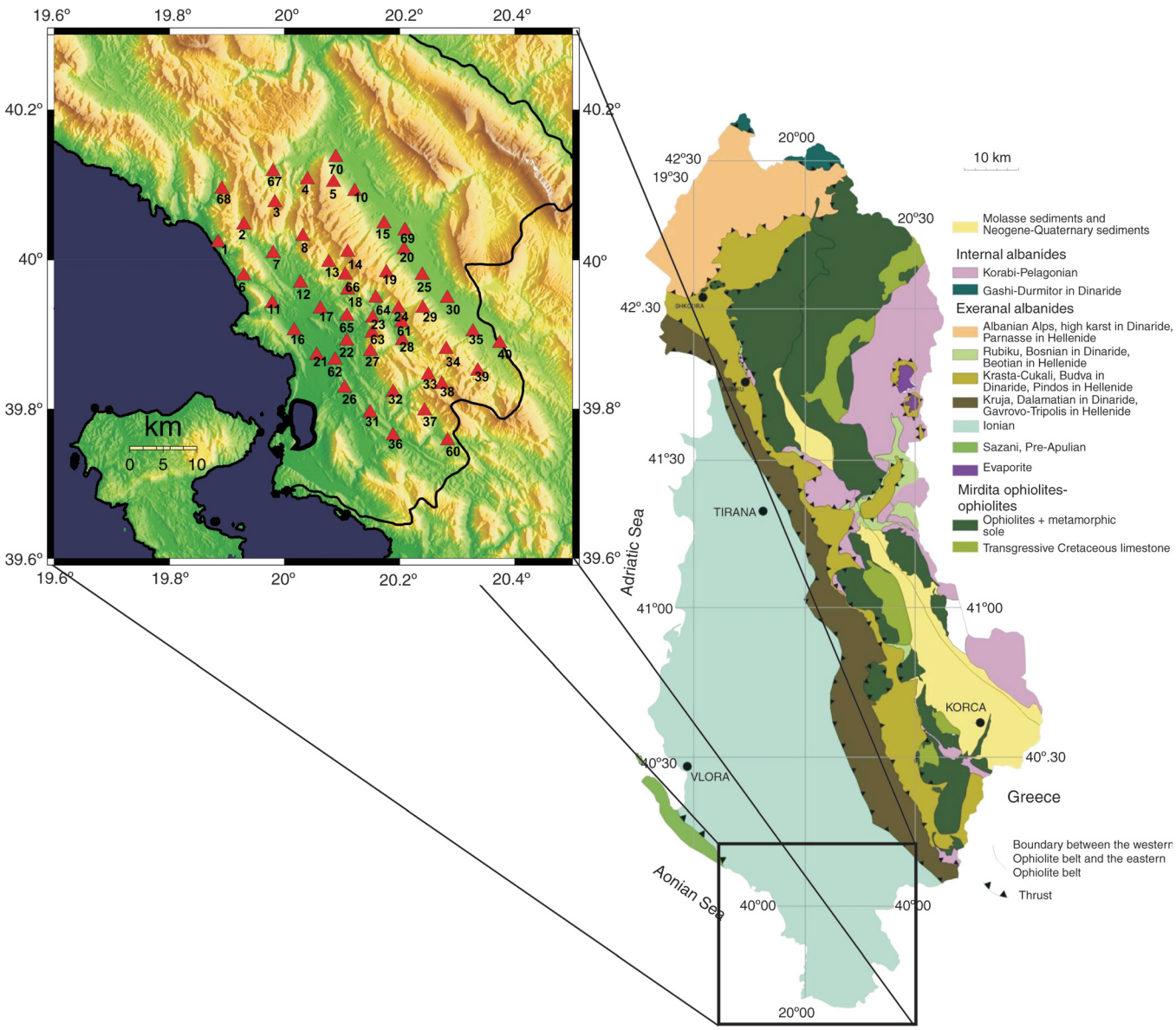

Figure 1. Geologic map of Albania. Close-up view depicts the topography of the area and the locations of the microearthquake stations (triangles) (adapted from Hoxha [2001]).

ID: thangabaluP Time: 13:22 I Path: Q:/3b2/GPY#/Vol00000/110059/APPFile/AI-GPY#110059

J_ID: GPY DOI: 10.1190/1.3560016 Date: 10-March-11 Stage: Page: 4 Total Pages: 24

sections are presented in Figure 4. In general, the seismicity was concentrated in small clusters; a higher concentration of epicenters was encountered toward the northwest and southwest parts of the area.

Magnitudes of the events ranged from 0 to 3 R (Richter scale), with most events occurring between 1 and 2 R (Figure 5a). Hypocentral depths were between 0 and 20 km, whereas most were located at depths of 2–10 km (Figure 5b). Most of the events were located using 10–30 P- and S-wave arrivals (Figure 5c), and their rms errors ranged from 0–0.15 s (Figure 5d). Most rise times (Figure 5e) were 0.015–0.06 s.

DATA PROCESSING

The data processing of a PST survey can be divided into three main steps. The first is estimating the best-fitting 1D initial velocity model in parallel with the optimization of the hypocenter locations. The second is the 3D velocity model construction. The third is related to the quality control (QC) of the results.

Estimating minimum 1D velocity model

The results and reliability of the 3D tomographic inversion, which is solved as a linear approximation of a nonlinear function, depend on the initial reference model.

The scope of this phase throughout an iterative joint hypocenter/velocity inversion is to identify the 1D model that minimizes the rms error of the hypocenters, following Kissling et al. (1994). We also check the quality of the 1D model following the procedure of Haslinger (1998). Based on that, we randomly perturb the calculated seismic events' hypocenter locations from 0 to 10 km on the x, y, and z axes. If the 1D model we use is reliable, after recalculating hypocenter parameters, the final locations will be similar to the original ones (<500 m). Otherwise, the difference will be larger, suggesting that 1D model reliability must be reconsidered.

In this case, the final locations for most relocated hypocenters were less than 150 m in the two horizontal directions but higher than 150 m in the vertical direction. The reliability of the 1D model was also tested by comparing event locations derived from traveltime data from the PST network to locations

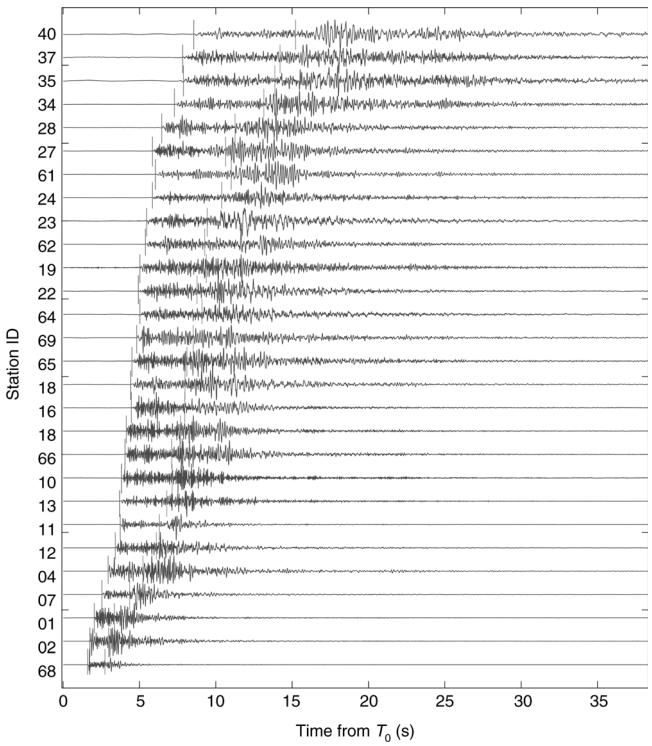

Figure 2. Example of a microearthquake as recorded by 28 stations of the network. Amplitudes are normalized and time is presented from the event's start time τ_0. The P- and S-wave arrivals are also displayed.

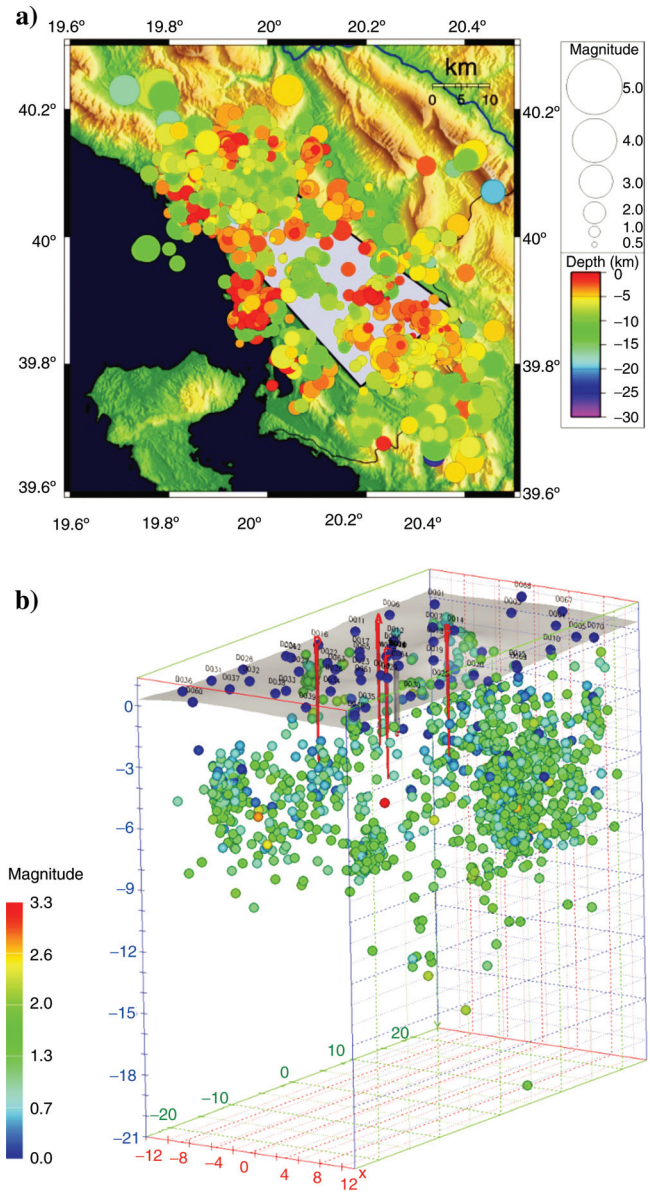

Figure 3. (a) Epicenters of recorded microearthquakes. (b) A 3D view of the hypocenters. Color scale shows magnitude distribution.

ID: thangabaluP Time: 13:23 I Path: Q:/3b2/GPY#/Vol00000/110059/APPFile/AI-GPY#110059

J_ID: GPY DOI: 10.1190/1.3560016 Date: 10-March-11 Stage: Page: 5 Total Pages: 24

provided by international seismological networks (e.g., European Mediterranean Seismological Centre and the U. S. Geological Survey).

As a starting model for the 1D velocity inversion, we used a reliable and well-tested initial velocity model derived from a similar survey in the adjacent area of Epirus in northwestern Greece (Kapotas et al., 2003). This area is located within the same tectonic zone (Ionian) with similar geotectonic characteristics (King et al., 1983; Martakis et al., 2006; Tselentis et al., 2006), so we expected this initial model would provide a reasonable approximation.

The 1D initial crustal model was used for a joint hypocenter/velocity inversion to fine-tune the model to the specific area of interest. The two areas are close and similar, so the new 1D model was almost exactly the same as the initial model. The 1D velocity model for P-wave velocity and V_P/V_S that was used in following inversion is presented in Table 1.

Estimating 3D velocity model

In this phase, we attempt to estimate the 3D velocity model and corresponding hypocenter parameters using the P- and

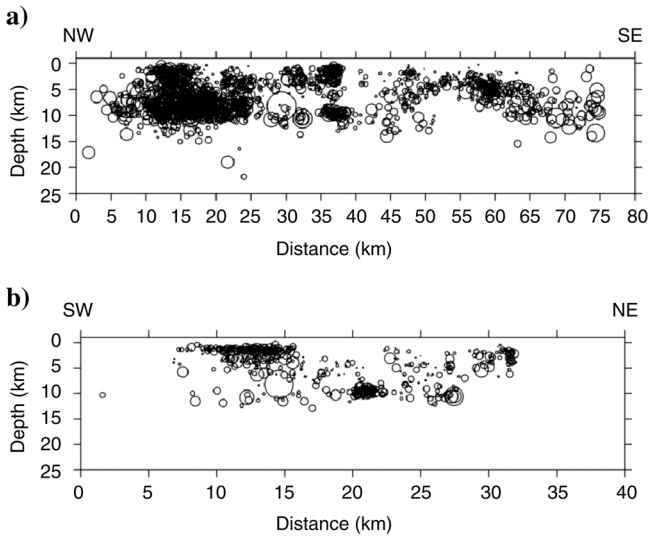

Figure 4. Depth cross section of seismicity distribution projected along (a) northwest–southeast and (b) southwest–northeast directions.

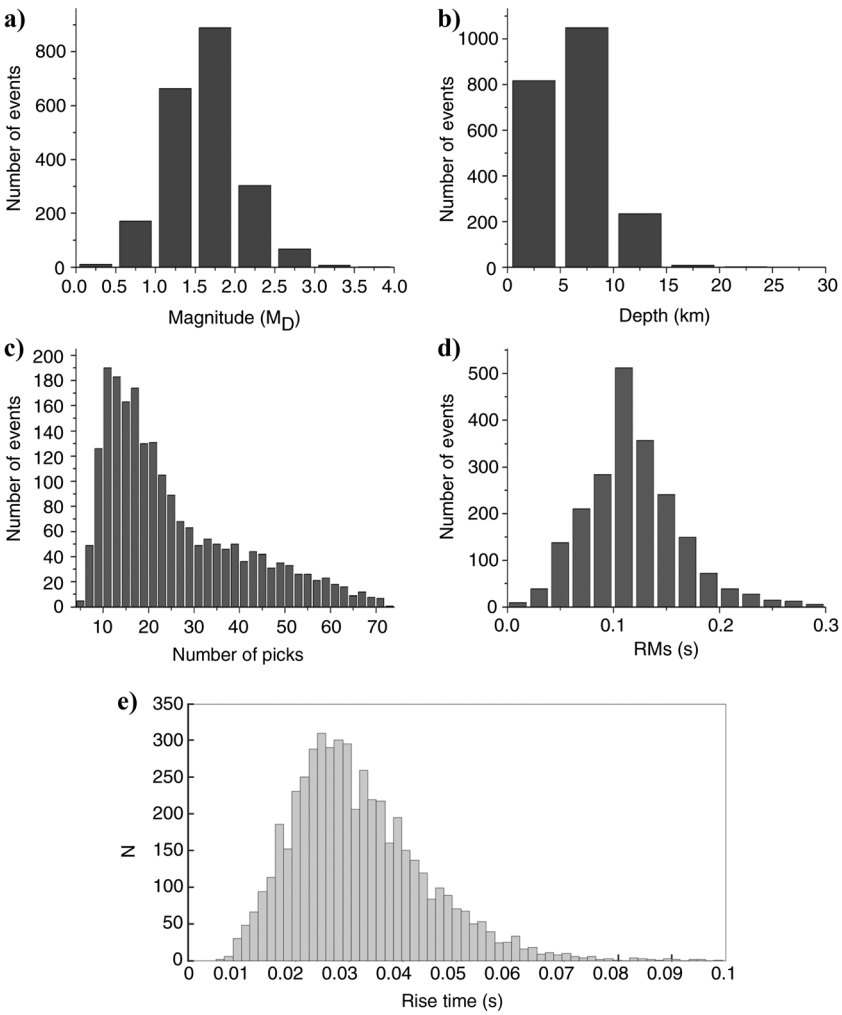

Figure 5. Histogram of (a) microearthquake magnitudes, (b) hypocenter depths, (c) number of peaks, (d) rms, and (e) rise times.

ID: thangabaluP Time: 13:24 I Path: Q:/3b2/GPY#/Vol00000/110059/APPFile/AI-GPY#110059

S-wave arrival times at the seismic stations and an initial estimate of the hypocenter locations and coordinates of the seismic stations.

The traveltime T_{ij} of a seismic wave from hypocenter i to receiver j is given by

$$T_{ij} = \int_{\text{source}}^{\text{receiver}} u\, ds, \tag{1}$$

where u is the slowness field and ds is a ray segment along the raypath (Thurber, 1983; Evans et al., 1994; Martakis et al., 2006). The arrival times τ_{ij} are given by

$$\tau_{\text{ij}} = \tau_i + T^s_{\text{ij}}(x_i, y_i, z_i, u(s), x, y, z), \tag{2}$$

where τ_i is the time of origin of the ith earthquake and where $(x_i,\ y_i,\ z_i)$ and $(x,\ y,\ z)$ are the coordinates of the source and receivers, respectively.

If $r_{ij} = \tau^{\text{obs}}_{ij} - \tau^{\text{calc}}_{ij}$ are the arrival-time residuals between the observed τ^{obs} and calculated τ^{calc} traveltimes, we end up with the following linear system of equations:

$$r_{\text{ij}} = \sum_1^3 \frac{\partial T_{\text{ij}}}{\partial x_{\text{k}}} \Delta x_{\text{k}} + \Delta \tau_{\text{i}} + \sum_1^L \frac{\partial T_{ij}}{\partial m_l} \Delta m_l, \tag{3}$$

Here, Δx_k and Δm_l are the perturbations to the hypocenter parameters and the velocity perturbations, respectively.

The partial derivatives in equation 3, with respect to the hypocenter parameters, are given by

$$\frac{\partial T_{ij}}{\partial x_k} = -\frac{1}{V}\left(\frac{dx_k}{ds}\right)_{\text{source}}, \tag{4}$$

as described by Lee and Stewart (1981). According to Thurber (1983), the partial derivatives with respect to the velocity model parameters are approximations of the path integrals, given by

$$\frac{\partial T_{ij}}{\partial m_l} = \int_{\text{source}}^{\text{receiver}} -1\left\{\frac{1}{V(x,y,z)}\right\}^2 \frac{\partial V(x,y,z)}{\partial m_i} ds. \tag{5}$$

Table 1. Minimum initial 1D velocity model for Delvina passive seismic tomography survey.

Depth (km)	V_{P} (km/s)	$V_{\text{P}}/V_{\text{S}}$
–2	4.90	1.78
0	5.12	1.78
2	5.33	1.78
4	5.52	1.78
6	5.62	1.78
8	5.82	1.78
10	6.05	1.78
15	6.25	1.78
20	6.39	1.78
30	6.50	1.78
40	8.00	1.78

The velocity $V(x,y,z)$ and its partial derivative with respect to a model parameter can be calculated through an interpolation scheme. The minimization of the traveltime residuals involves solving the forward and inverse problems during an iterative process. The forward problem can be written in matrix notation as

$$\Delta \mathbf{d} \approx \mathbf{G}\Delta \mathbf{m}, \tag{6}$$

where $\mathbf{G}$ is the Jacobian matrix containing all of the partial derivatives in equation 3, $\Delta\mathbf{d}$ are the residuals, and $\Delta\mathbf{m}$ are the perturbations of the model parameters. Because the problem of passive tomography is usually underdetermined or mixed determined, the damped least-squares method is applied:

$$\Delta \mathbf{m} = \left(\mathbf{G}^T\mathbf{G} + \varepsilon^2\mathbf{I}\right)^{-1}\mathbf{G}^T\Delta\mathbf{d}, \tag{7}$$

where ε^2 is the damping factor.

The updated velocity model was used to again calculate the hypocenter parameters, trying to minimize the residual traveltimes of the predicted traveltimes from the observed ones. The updated hypocenter parameters were then used for a new iteration to improve the velocity model.

PATOS2-LandTech tomographic inversion software was used to perform all of the calculations. The parameterization of the problem was based on the 3D grid of nodes technique. To solve the forward problem, two ray-tracing algorithms were used and tested: approximate ray tracing (ART) and pseudobending (Um and Thurber, 1987) and Runge-Kutta + perturbation (RKP) shooting ray tracing (Virieux, 1991). For this study area, we preferred ART and pseudobending.

In the case of the Delvina PST survey, we applied the above-mentioned procedures, checking different damping and gridding parameters to provide a reliable and robust 3D model without sacrificing its resolution. The trade-off curves for damping the value estimation showed that the optimum damping factors were 20 for V_{P} and 10 for $V_{\text{P}}/V_{\text{S}}$.

Different parameterization schemes also were applied. Based on the geometry of the seismic network and the distribution of hypocenters, the optimum result was derived using a $2 \times 2 \times 1$-km (along the x-, y-, and z-axes) grid spacing on a linear B-spline interpolation scheme with values every 100 m. Although efforts were made to minimize the grid spacing further, the seismic events were distributed unevenly, with distances between stations of approximately 5 km; the resulting model showed undesirable velocities and oscillations. In our research, a $2 \times 2 \times 1$-km grid spacing was eventually selected for interpretation. The processing steps are shown in Figure 6.

The seismic events used to construct the model provided 47,280 P- and S-wave arrivals (24,438 P-wave and 22,842 S-wave) for the tomographic inversion to estimate 25,076 V_{P} and $V_{\text{P}}/V_{\text{S}}$ parameters. Five iterations were performed, at which point the rms error was sufficiently low. For the rms to be considered sufficiently low, two criteria are used: The model variance must be very low or stable, and the rms with the iteration number curve must be almost flat or show small change. The rms of the final model was 0.0964, which was reduced by 21.5% from the starting value of 0.1228. The final total rms for seismic events using hypocenter estimation was 0.070, which was reduced by 39.1% from a starting value of 0.115. The reliability of the inversion result should not be limited to the rms values but should be examined further (Appendix A).

J_ID: GPY DOI: 10.1190/1.3560016 Date: 10-March-11 Stage: Page: 7 Total Pages: 24

Estimating 3D Q_P model

A mathematical model for realistic pulse broadening in an inhomogeneous medium has been suggested by Gladwin and Stacey (1974) and Stacey et al. (1975). These studies show experimentally that the rise times of acoustic signals propagating linearly in elastic media with frequency-independent quality quotient Q is described by

$$\tau = \tau_0 + \mathrm{C}\int_{\mathrm{ray}} \frac{ds}{V_p Q} = \tau_0 + \mathrm{C}\int_{\mathrm{ray}} \frac{\Delta T}{Q}, \tag{8}$$

where τ is the pulse rise time, τ_0 is the original pulse rise time at the source, C is a constant, ds is an arc segment along a raypath, and ΔT is the incremental traveltime.

The pulse rise time is the amplitude of the first-arriving pulse divided by the steepest rising slope. The rise time, defined in displacement records, is approximately the pulse width on velocity seismograms (Zucca et al., 1994). This parameter is defined as the time difference from the onset of the initial arrival to the initial peak for displacement seismograms or, equivalently, from the onset to the time at which zero is crossed for the first time in velocity records. The error introduced by misspeaking can be large for short pulse widths, so we use the time between the linear extrapolations of the rising slope at half peak (Figure 7a) to the time axis and the first zero crossing (Zucca et al., 1994).

Figure 7b shows an increase in the observed rise times with increasing hypocenter distance, which indicates that attenuation increases with hypocenter distance and that the rise-time model can be used in this study area.

For a medium with constant V_P, where $Q = Q_0$, equation 8 can be written in a linear form:

$$\tau = \tau_0 + \frac{CT}{Q_0}. \tag{9}$$

The ratio T/Q is usually referred as t^* (t star) in the literature. The constant C was determined experimentally for ultrasonic acoustic pulses to be 0.5 (Gladwin and Stacey, 1974). A theoretical demonstration, based on an impulsive displacement source, is given by Kjartansson (1979).

Other investigations (Blair and Spathis, 1982; Liu, 1988; Wu and Lees, 1996; Tselentis, 1998) show that C depends on the shape of the source-time function. In the case of small events, a C value of 0.5, which corresponds to an impulsive displacement function, is commonly used (de Lorenzo et al., 2004). This is because first-arrival velocity pulses for microearthquakes appear closest in shape to derivative Gaussian pulses, which correspond to Gaussian function displacements.

Obviously, the most limiting assumption of the method for estimating Q_P is that it neglects the directivity effect of the seismic radiation generated by a finite dimensional seismic source (Zollo and de Lorenzo, 2001; Tselentis et al., 2010).

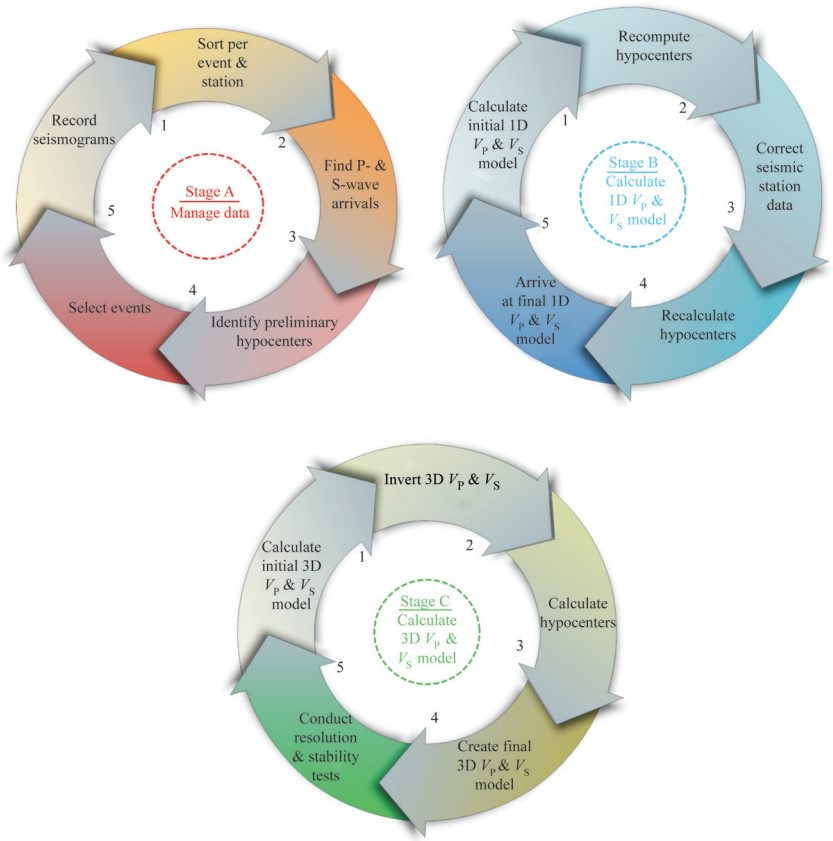

Figure 6. Data processing stages for obtaining the 3D velocity structure of the region.

ID: thangabaluP Time: 13:25 I Path: Q:/3b2/GPY#/Vol00000/110059/APPFile/AI-GPY#110059

J_ID: GPY DOI: 10.1190/1.3560016 Date: 10-March-11 Stage: Page: 8 Total Pages: 24

Because our methodology does not use amplitude information, we did not perform the deconvolution for the instrumental response. Furthermore, the histogram of the observed rise times shows that most values lie between 0.015 and 0.06 s (Figure 5e), indicating an average frequency content ranging from 3 to 40 Hz. In this frequency band, the response of the equipment used is flat and cannot distort the duration and shape of the observed signals.

The first step in Q_P model inversion is to estimate the initial rise time for each event. Because each event has a different initial pulse width τ_0, there is one τ_0 value per event. After the picking was completed, we plotted the values of the rise times for each event against the P-wave-arrival traveltimes (Figure 7c). A straight line was fitted to the data points using the least-squares method. The point where the line intersected with the rise-time axes (equation 9) was used to determine the value of τ_0 used for that event. From equation 9, we can write

$$\tau - \tau_0 = C \int_{ray} \frac{1}{Q_p V_P} ds. \quad (10)$$

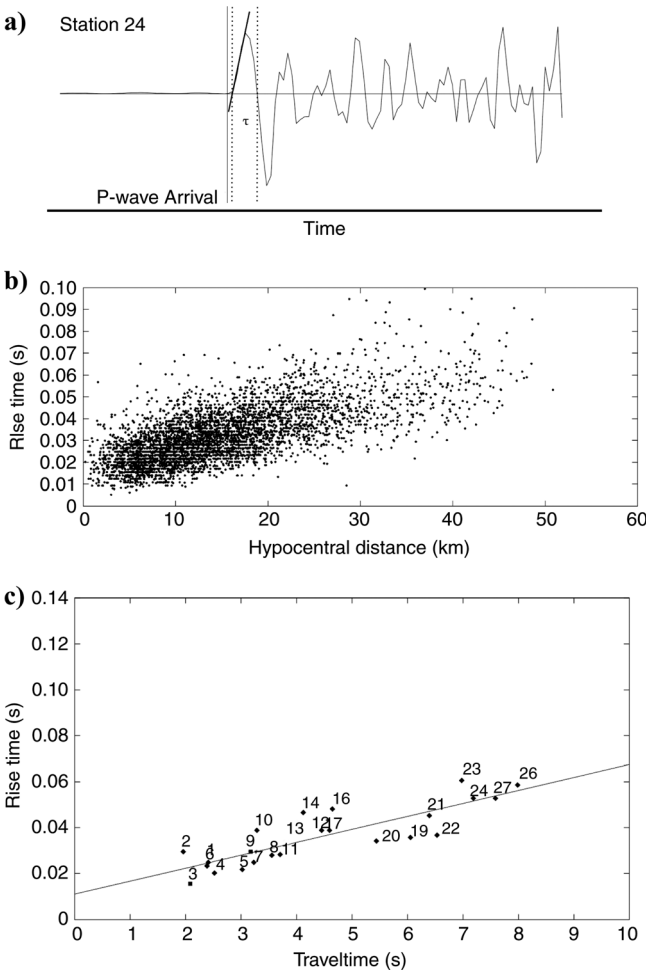

Figure 7. (a) Measurement of rise time and pulse-width broadening for a single event recorded at station 24. The start of the pulse (solid line), the end of the rise time (dashed line), and the pulse width (dotted line) are shown. (b) Increasing rise times with increasing hypocenter distance. (c) Plot of measured rise times for a selected event in order to estimate τ_0.

As made clear in equation 10, it is important to have an accurate P-wave velocity model (Q_P is the target parameter) to apply the method for estimating Q_P. The nonlinear tomographic analysis of the P-wave arrival times provided a 3D P-wave velocity model as well as the raypaths from the hypocenter of each event to the recording stations.

In a process similar to velocity tomography, equation 10 was parameterized in discrete blocks, within which attenuation was assumed to be constant (Tselentis et al., 2010). In selecting the block dimensions, there was a trade-off between the higher resolution of the model and sufficient raypath coverage. The linear inversion for Q_P was accomplished following the same methodology as that used for the velocity inversion (Tselentis et al., 2010).

PST RESULTS

The inversion resulted in the form of horizontal and vertical cross sections for V_P and V_P/V_S that are presented in the following discussion. The horizontal sections were constructed every 500 m, starting from mean sea level, and the vertical sections were constructed every 4 km. Vertical cross sections of V_P and V_P/V_S values obtained from the seismic tomography results are calculated along the directions shown in Figure 8. Lines OO′ and PP′ represent the cross sections passing through wells D4–D10 and D4–D12, respectively (Figure 8).

In this paper, we do not conduct a detailed geologic/lithologic interpretation of the PST results. The quantitative interpretation of PST results in relation to the properties of hydrocarbon reservoirs is a complicated task beyond the scope of the present text. Instead, we present some general conclusions and try to

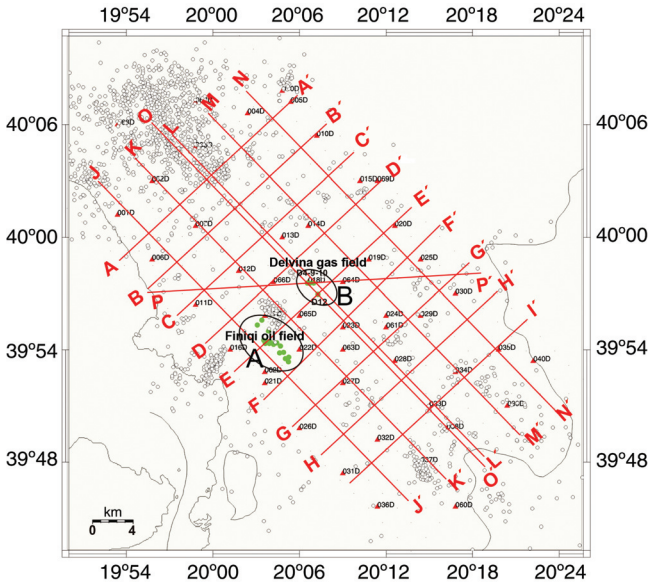

Figure 8. Directions along which vertical tomographic sections have been compiled. The positions of existing wells and the location of the (A) oil- and (B) gas-producing areas are also presented.

ID: thangabaluP Time: 13:26 I Path: Q:/3b2/GPY#/Vol00000/110059/APPFile/AI-GPY#110059

J_ID: GPY DOI: 10.1190/1.3560016 Date: 10-March-11 Stage: Page: 9 Total Pages: 24

correlate the seismic tomography sections with the general features of the oil and gas fields.

Figure 9 compares the V_P cross section obtained along line DD′ (Figure 8) with a geologic model given by the Albanian National Agency of Hydrocarbons (Luan et al., 2001; Velaj, 2001), based on well data and in part on poor-quality conventional seismic results. It is obvious that the geologic information and PST results were very similar. Starting from the west, the low velocities (arrow a) correspond to Quaternary and flysch deposits, whereas high velocities (arrow b) fit very well with Cretaceous, Jurassic, and Tertiary outcrops toward the northwestern part of the investigated region. The anticline (arrow c) is also reconstructed very well, and the evaporitic flysch (arrow d), T3 Tertiary dolomite (arrow e), and Jurassic carbonate (arrow f) layers correlate well with the velocity section from PST. This correlation is presented as an additional quality control (QC) test and not for interpretation reasons.

Although the Delvina area has been widely explored since 1980 and there have been oil and gas discoveries in the region, the most significant information about its structural and lithological regime was derived partially from well data and surface geology. Conventional seismic sections were of very poor quality because of severe seismic penetration problems, the complicated overthrust geotectonic regime, and the presence of evaporitic structures. Thus, conventional 2D seismic results could not be used to identify and characterize the structural regime of the area.

Figure 10 presents horizontal V_P sections at a depth spacing of 500 m, whereas Figures 11 and 12 depict vertical V_P sections along the direction shown in Figure 8. Similar sections for V_P/V_S are shown in Figures 13 and 14.

Apart from the structural information given by the V_P and V_P/V_S sections, some lithologic information can be obtained. It is known (Hamada, 2004) that V_P is sensitive to type of saturation fluid, so V_P/V_S is a good tool for identifying fluid type. The fact that V_P decreases and V_S increases with increases in light hydrocarbon saturation makes V_P/V_S more sensitive to changes of fluid type than using V_P or V_S separately.

Finally, Figure 15 presents horizontal Q_P sections, resulting from the inversion of the rise times at a depth spacing of 1000 m.

Gas field

In this section, we present an interpretation of PST results by correlating the results with preexisting geological, geophysical, and well data, focusing mainly on the Delvina gas field.

In Figures 16 and 17, the correlation between PST and preexisting data is presented at 2 and 3.5 km, respectively. In both figures, most of the structures correlate well with the PST data (Ftera-Fitore and Maligere anticlines and Vurgut syncline, as shown in Figure 10).

Figure 18 presents a 3D view of the Delvina anticline structure and the surrounding structures as produced using PST results. The Delvina anticline is adjacent to the Ftera-Fitore anticline to the west.

Next, we focus on the production area of the Delvina gas field (region B on Figure 8; wells D4, D9, D10, and D12) to provide a brief interpretation of the PST results. Figure 19 shows the V_P and V_P/V_S cross sections along wells D4–D12 (OO′ in Figure 8) and focuses on the corresponding results between 18 and 32 km (Figure 19b and d), a region believed to correspond to the gas-production zone. The V_P and V_P/V_S sections and the 3D model (Figure 18) show that although the PST models were constructed for an area of approximately 1000 km^2, they correlate satisfactorily with well data and can be used to delineate the structure of the reservoir.

The bottom of the flysche layer, which acts as a top seal of the gas reservoir obtained from the PST survey, corroborates the well findings. A production zone spanning between 21 and 26 km with a thickness of 0–700 m above the water-oil contact (WOC) can be delineated. Well D12, characterized by high production, was located toward the center of the Delvina anticline; well D4, characterized by much less production, was located near the left border of the region (Figure 18). A secondary anticline structure with characteristics similar to the neighboring production zone was also identified (denoted by the dashed line in Figure 19b and d) and will be tested by a new well.

Figure 20 presents the V_P and V_P/V_S PST results along the PP′ direction (Figure 8), with inserts showing the region between 12 and 22 km (Figures 20b and d). The only well that was difficult to correlate with the seismic tomography result was D10. In this well, which was not producing at the time of the study, the V_P/V_S at the target depth (3.5 km) was close to 1.8, which is higher than the values (<1.75) observed for wells D4 and D9, which were producing.

Low V_P/V_S values characterize gas-bearing rocks (i.e., those with a high fluid compressibility), whereas higher values of V_P/V_S indicate liquid-bearing formations (i.e., those with a low fluid compressibility). Furthermore, pore-fluid pressure may also play a role by inducing a fluid-phase transition and by keeping pores and cracks open. As a consequence, velocities are further affected. Using laboratory measurements and effective medium modeling, Dvorkin and Nur (1996) show that crack opening induced by increasing pore pressure leads to a strong reduction in V_P/V_S in gas-bearing rocks.

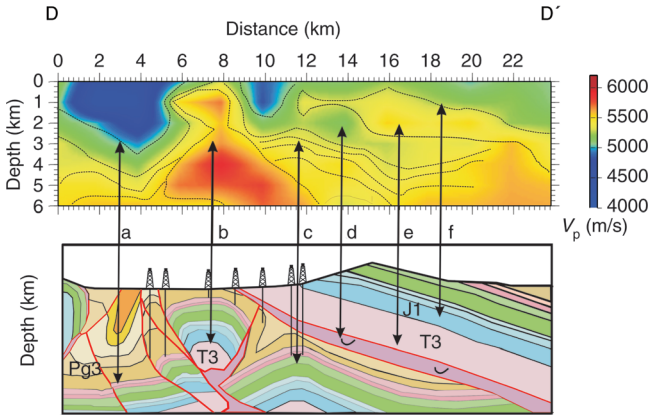

Figure 9. Comparison of a general geological section along line DD′ (in Figure 8) and the derived V_P velocity model from the PST survey. (a) Low velocities correspond to Quaternary and flysch deposits. (b) High velocities fit well with Cretaceous, Jurassic, and Tertiary outcrops toward the northwestern part of the investigated region. (c) The anticline is reconstructed very well. (d) The evaporitic flysch, (e) T3 Tertiary dolomite, and (f) Jurassic carbonate layers also correlate well with the velocity section from PST. This correlation is an additional QC test and not for interpretation; thus, only main structures are compared with the arrows.

ID: thangabaluP Time: 13:26 I Path: Q:/3b2/GPY#/Vol00000/110059/APPFile/AI-GPY#110059

J_ID: GPY DOI: 10.1190/1.3560016 Date: 10-March-11 Stage: Page: 10 Total Pages: 24

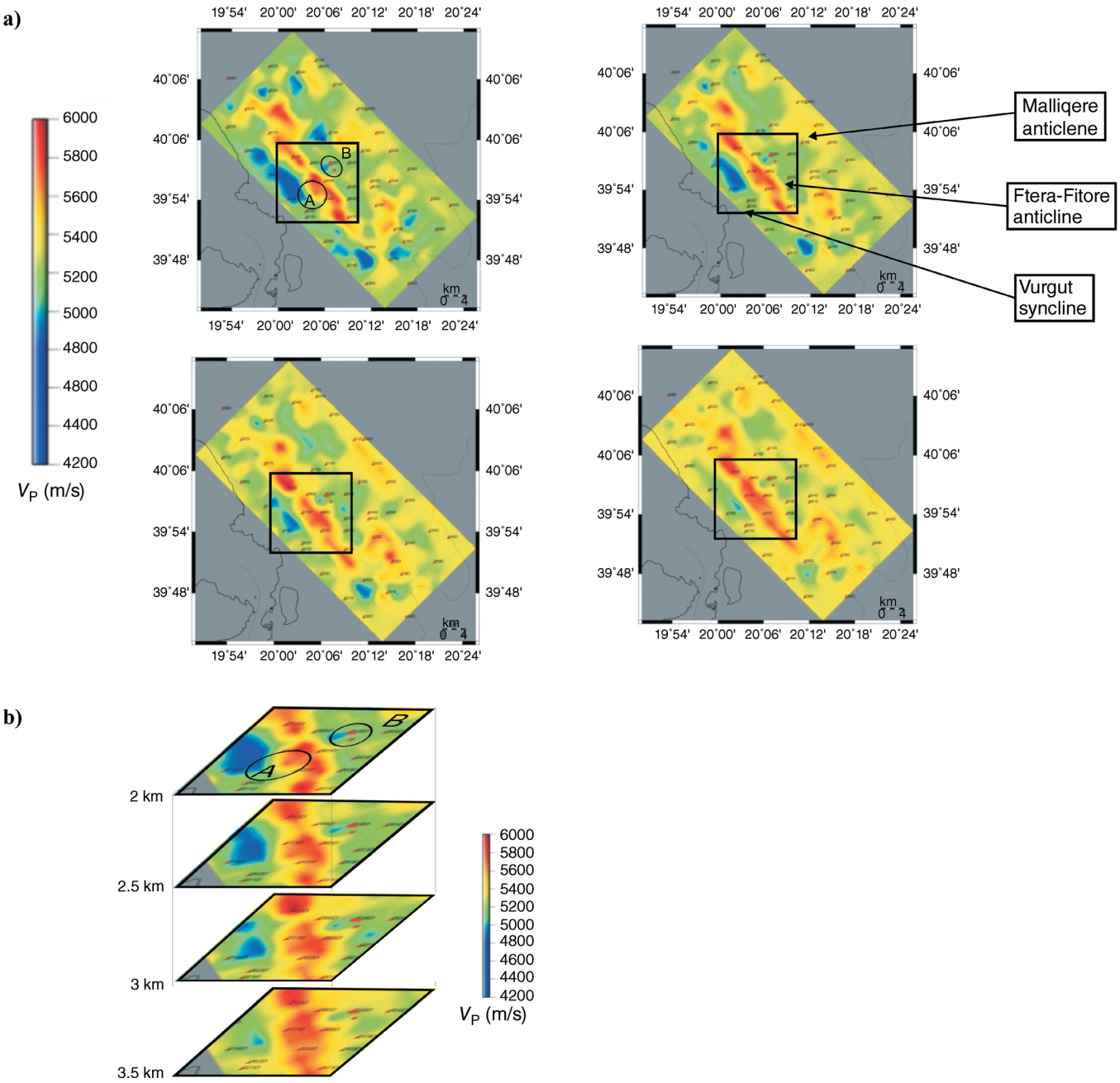

Figure 10. (a) Horizontal V_P sections of the investigated area spaced at 500 m. Damping is 30 and grid spacing is 1000 m for all views. Depth is (upper left) 2 km, (upper right) 2.5 km, (lower left) 3.0 km, and (lower right) 3.5 km. (b) Enlarged V_P section for the production interval from 2 to 3.5 km. Ellipses A and B correspond to regions of known oil and gas reservoirs, respectively.

ID: thangabaluP Time: 13:26 I Path: Q:/3b2/GPY#/Vol00000/110059/APPFile/AI-GPY#110059

J_ID: GPY DOI: 10.1190/1.3560016 Date: 10-March-11 Stage: Page: 11 Total Pages: 24

Figure 21 presents the values of V_P/V_S versus V_S and V_P, respectively, obtained for the gas field and at various depths on figure, what are the units for Vp – km/s?. Judging from this diagram, we can see that at the depth of the gas-field reservoir (~3 km), the V_P/V_S values reached a minimum, as expected from the literature. The V_P value for well D10 at the target depth was slightly higher than that for wells D4 and D9 (Figure 20b). Well D9 had higher production than well D4, probably because it is crestal to the structure (Figures 20a and b).

The physical parameters of many rocks contribute to changes in seismic velocities of rocks in addition to mineralogy, porosity, and in situ stress conditions such as pore-fluid properties, which in turn depend on temperature and pressure (Vanorio et al., 2005). It is well known that the content and physical state of fluids affect P-wave velocities more strongly than S-wave velocities. Figure 22 presents the variation of V_P versus V_S for the gas-field reservoir region (~3 km) at various depths overlaid on empirical curves estimated for different lithologies (Castagna et al., 1985, 1993).

Decreases of Q_P in rocks (Winkler and Nur, 1979) reportedly have been caused by partial saturation (i.e., gas-liquid mixture). This seems to agree with the results obtained by the attenuation tomography in our investigation. Figure 15 shows that in the region of the gas field, we obtain lower values of Q_P than expected.

Oil field

Toward the southwestern end of the investigated area is a well-known oil-producing reservoir, shown as region A in Figure 8. In this section, we attempt to explain the results of the PST analysis in relation to this reservoir.

Figure 23 presents V_P and V_P/V_S cross sections, respectively, along line EE′ (Figure 8) are there units for Vp/Vs on Figure 23?. This line passes through the Finiq oil field and well D-12, and it was selected for interpretation because the oil field is very well defined and can be used for calibration. In the V_P and, especially, the V_P/V_S sections, the carbonate top is estimated

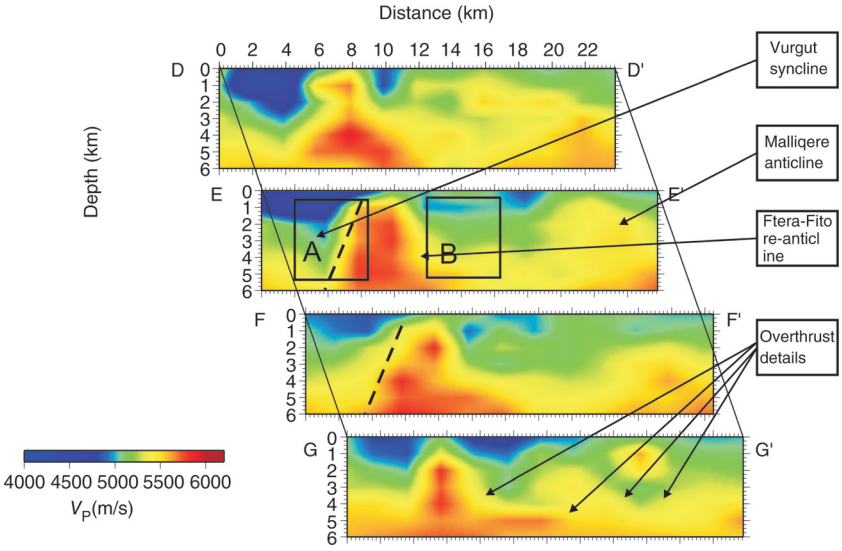

Figure 11. Vertical V_P sections along the southwest–northeast lines depicted in Figure 8. Known synclines and anticlines are also shown. A = oil field; B = gas field.

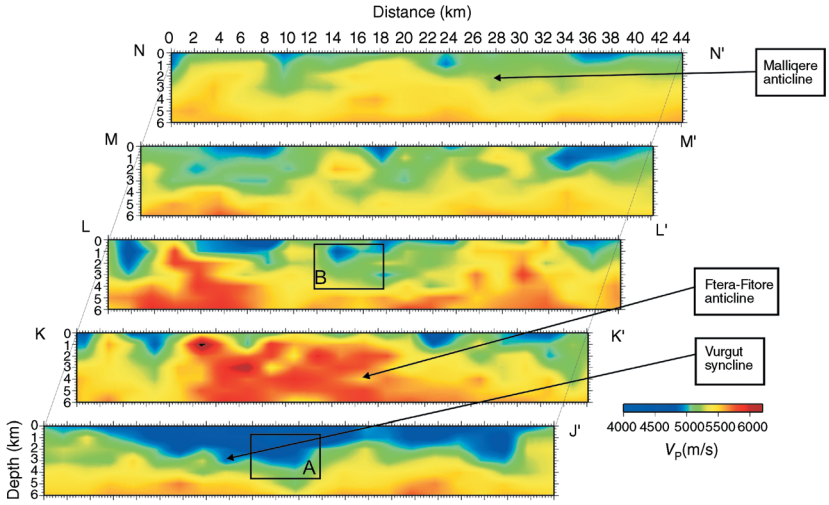

Figure 12. Vertical V_P sections along the northwest–southeast lines depicted in Figure 8. A = oil field; B = gas field.

ID: thangabaluP Time: 13:28 I Path: Q:/3b2/GPY#/Vol00000/110059/APPFile/AI-GPY#110059

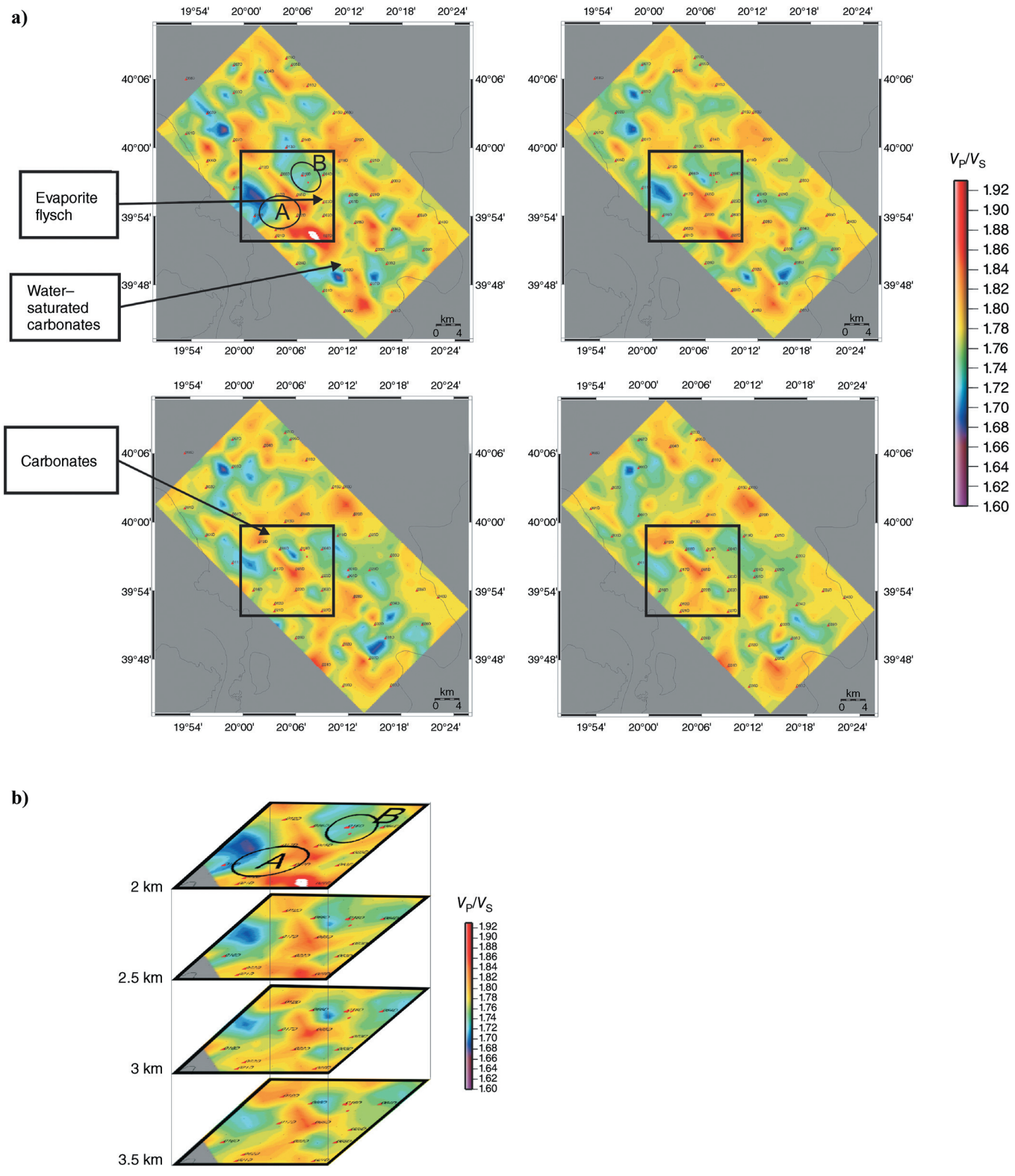

Figure 13. (a) Horizontal V_P/V_S sections of the investigated area spaced at 500 m. Damping is 10 and grid spacing is 1000 m for all views. Depth is (upper left) 2 km, (upper right) 2.5 km, (lower left) 3.0 km, and (lower right) 3.5 km. (b) Close-up of the V_P/V_S section for the producing depth interval from 2 to 3.5 km. A = oil field; B = gas field.

J_ID: GPY DOI: 10.1190/1.3560016 Date: 10-March-11 Stage: Page: 13 Total Pages: 24

well from the PST results at depths of 1300–1600 m and in Delvina at depths of 2800–2900 m.

Figure 24 depicts the obtained values of V_P/V_S versus V_S and V_P, respectively, for the oil-producing region at various depths. At the depth where the oil reservoir is encountered (~2 km), the V_P/V_S values reach a maximum value, which contradicts the minimum values obtained for the gas field. Figure 25 presents the relationship between V_P and V_S values, which were obtained from the passive survey but only for the corresponding production depths of the gas and oil reservoir. Despite the overlapping region, there is a tendency for the oil and gas values to separate from each other on the crossplot, which is more obvious in Figure 26, where the relationships between V_P/V_S and V_P and between V_P/V_S and V_S are plotted.

Similar to the results observed in the gas field, lower Q_P values were also observed in the oil field (Figure 15); and in the eastern limit of the oil field, a sharp Q_P contrast was observed. This is consistent with similar contrasts observed in the V_P and V_P/V_S tomographic results (Figure 13). These results mark an abrupt change in the lithology and/or saturation of the rocks. In the gas field, the western limit is marked by a less-pronounced contrast in the geophysical parameters.

LITHOLOGICAL CLASSIFICATION WITH KOHONEN NEURAL NETWORKS

SOM theory

To analyze the clustering of the data and to reveal the major lithological units in the region further, we use Kohonen self-organizing maps (SOMs). These unsupervised artificial neural networks developed by Kohonen (1995) are intended to provide ordered feature maps of input data after clustering (Ripley, 1996; Vesanto et al., 1999; Chang et al., 2002). In other words, SOMs are capable of mapping high-dimensional, similar input data into clusters close to each other on an n-dimensional grid of neurons (units).

This grid is the SOM map and is known as the output space, whereas the input space is the original space where the data patterns that we want to discover (in this case, volumes with similar properties) exist. This mapping tries to preserve topological relations (Villmann et al., 1997), i.e., patterns that are close in the input space will be mapped to neurons that are close in the output space, and vice versa. To provide even distances between units in the output space, hexagonal grids are often used (Bacao et al., 2005).

A basic distinction between classical neural networks and SOMs is the latter's ability to perform unsupervised learning. SOMs require no a priori information to function, and they excel at establishing unseen relationships in data sets (Penn, 2005). Once a SOM is trained for a specified data set, it can be applied to similar data sets.

The SOM training process for a given input pattern begins by calculating the Euclidian distance between that pattern and every unit in the network the winning unit is the one with the smallest distance and accept that the pattern is mapped onto that unit. If the SOM has been trained successfully, then patterns close in the input space will be mapped to neurons close in the output space, and vice versa.

The overall learning process of a SOM is accomplished through the iterative process depicted in Figure 27. Fitting of model vectors m_i is performed by sequential regression. The best match for each sample (index c) is subject to the condition

$$\forall i, \quad \|x(t) - m_c(t)\| \le \|x(t) - m_i(t)\|, \tag{11}$$

where t is the step index for each observation vector x. Then, all model vectors (or a subset of them) that belong to nodes around node $c = c(x)$ are updated by the relation

$$m_i(t+1) = m_i(t) + h_{c(x),i}[(x(t) - m_i(t))]. \tag{12}$$

In this formula, $h_{c(x),i}$ is the neighborhood function, which decreases with increasing separation between the ith and cth nodes on the map grid. This regression is reiterated over the available samples (Kohonen, 1995) to find the optimal index c.

To extract information from the SOM, the U-matrix is frequently used. This is a representation of the SOM, depicting the average distance of each node with its neighboring nodes. If

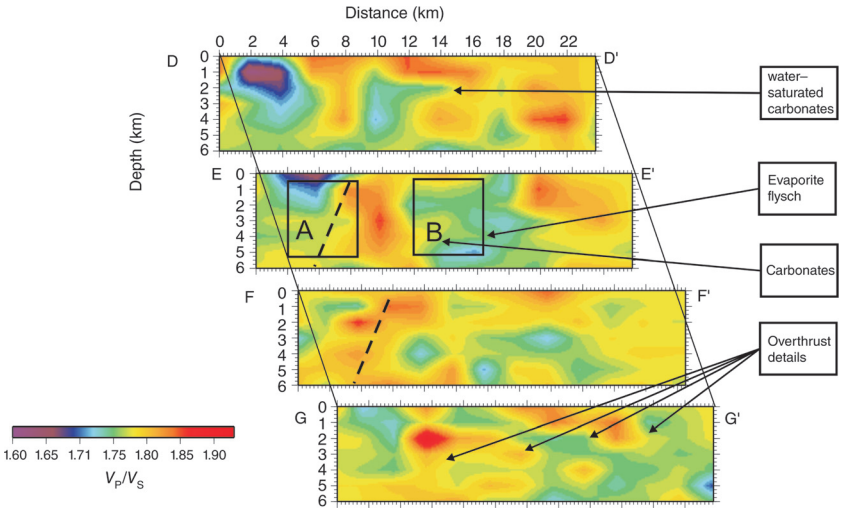

Figure 14. Vertical V_P/V_S sections along the southwest–northeast lines depicted in Figure 8. A = oil field; B = gas field.

ID: thangabaluP Time: 13:30 I Path: Q:/3b2/GPY#/Vol00000/110059/APPFile/AI-GPY#110059

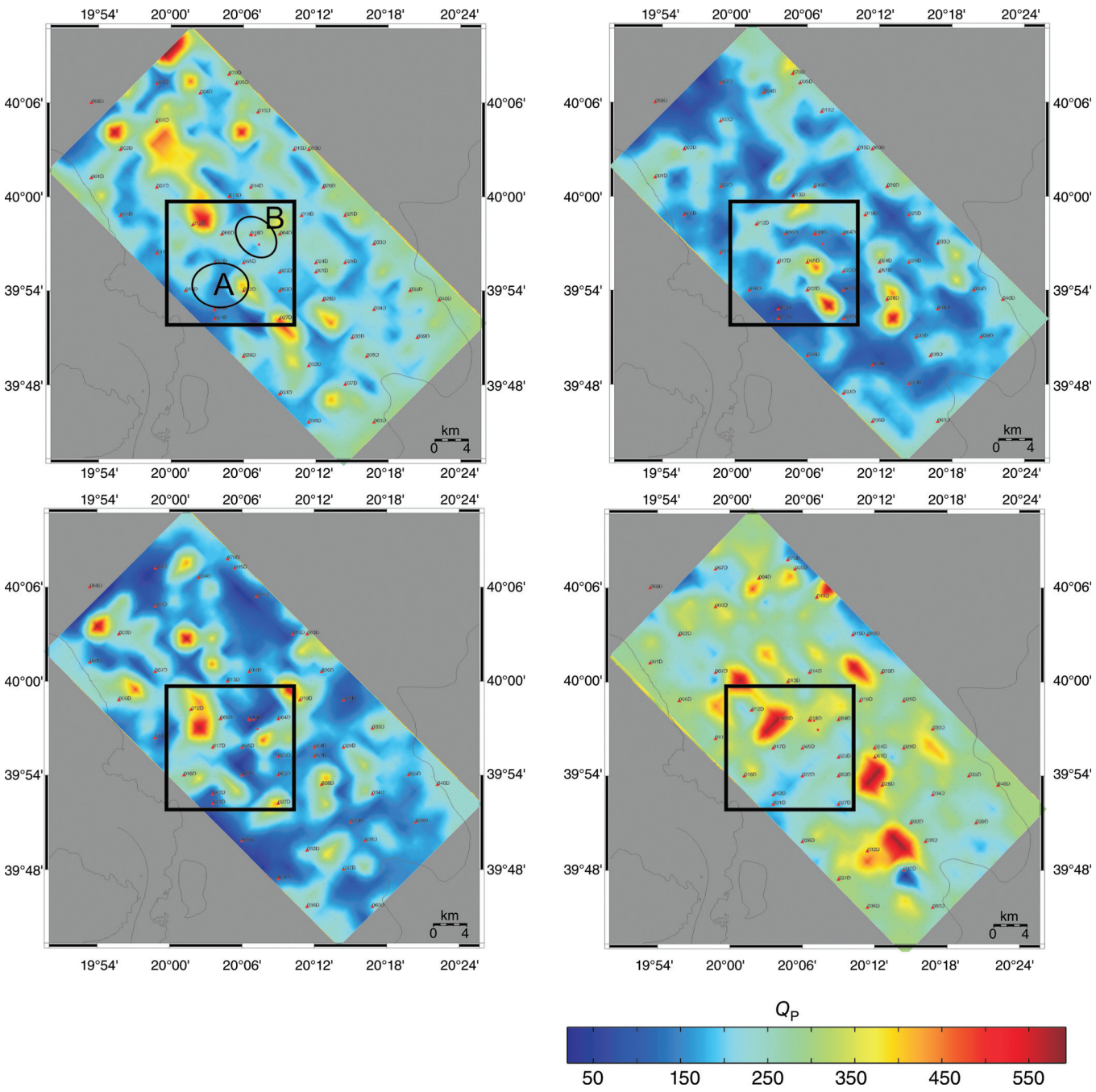

Figure 15. Q_P horizontal sections of the investigated area at a depth interval of 1000 m. Depth is (upper left) 1.5 km, (upper right) 2.5 km, (lower left) 3.5 km, and (lower right) 4.5 km. A = oil field; B = gas field.

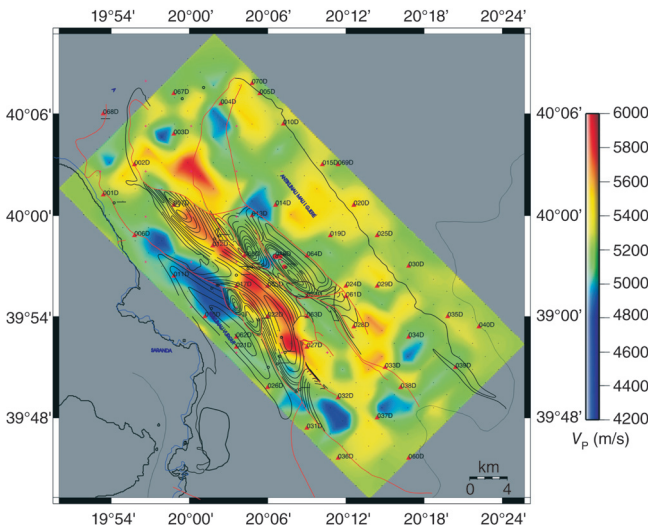

Figure 16. Correlation between preexisting data interpretation and PST results at 2 km depth (from mean sea level). Contours depict known depths to the limestone. Damping is 2 km; grid spacing is 1000 m.

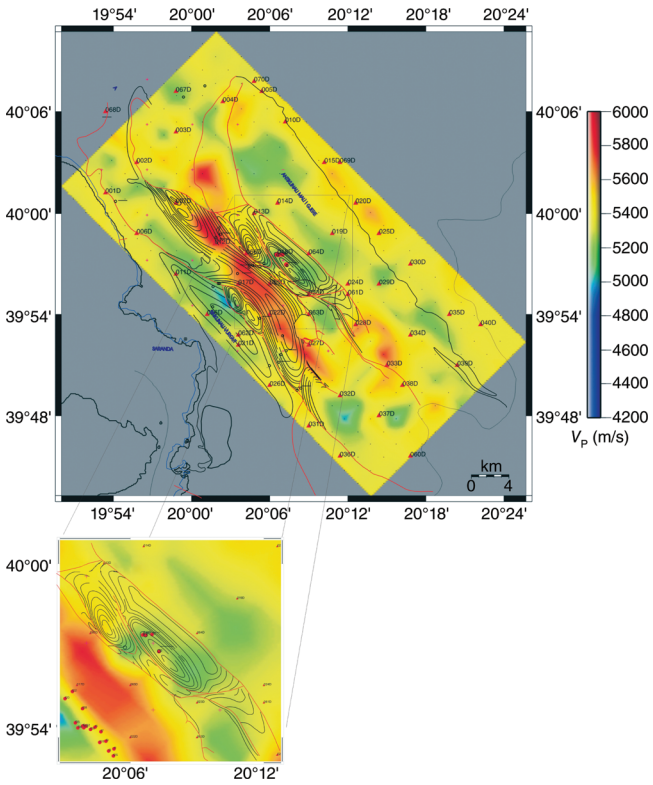

Figure 17. Correlation between preexisting data interpretation and PST results at 3.5 km depth (from mean sea level), focusing on the Delvina gas-production area. Contours depict depth to the limestone. Damping is 3.5 km; grid spacing is 1000 m.

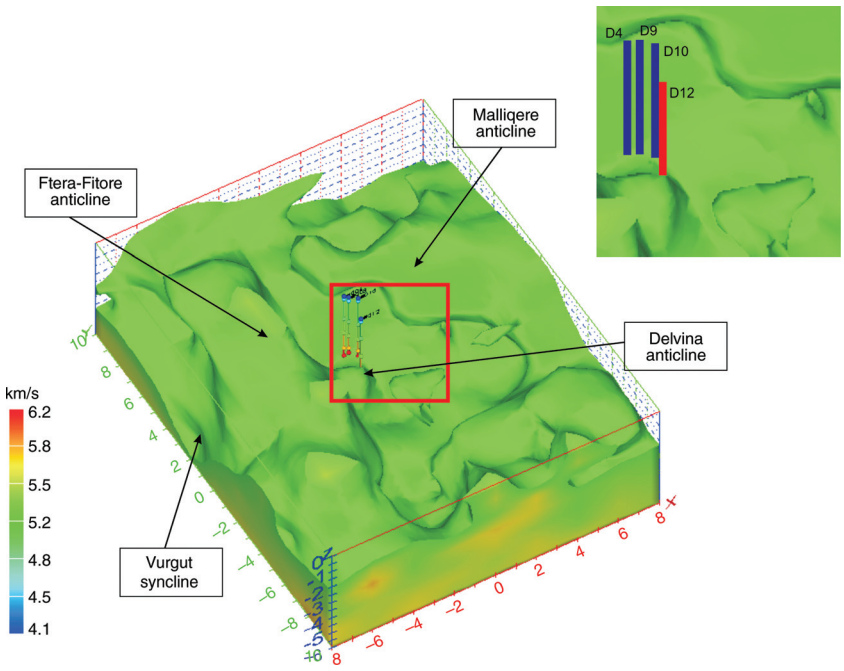

Figure 18. A 3D view of the Delvina anticline structure and surrounding structures based on PST results ($V_P > 5.24$). (upper right) Close-up view of a section of the structure.

J_ID: GPY DOI: 10.1190/1.3560016 Date: 10-March-11 Stage: Page: 16 Total Pages: 24

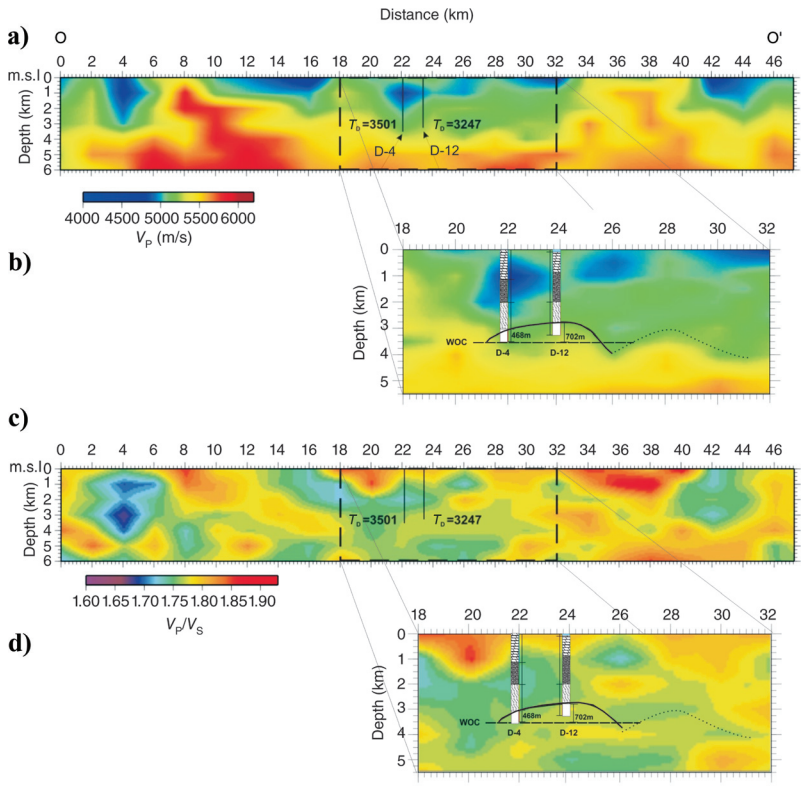

Figure 19. (a) V_P cross sections along line OO′. (b) Comparison with wells D-4 and D-12. (c) V_P/V_S cross sections along line OO′. (d) Comparison with wells D-4 and D-12. Dashed line labeled WOC is the water-oil contact. The dotted line presents a possible second anticline.

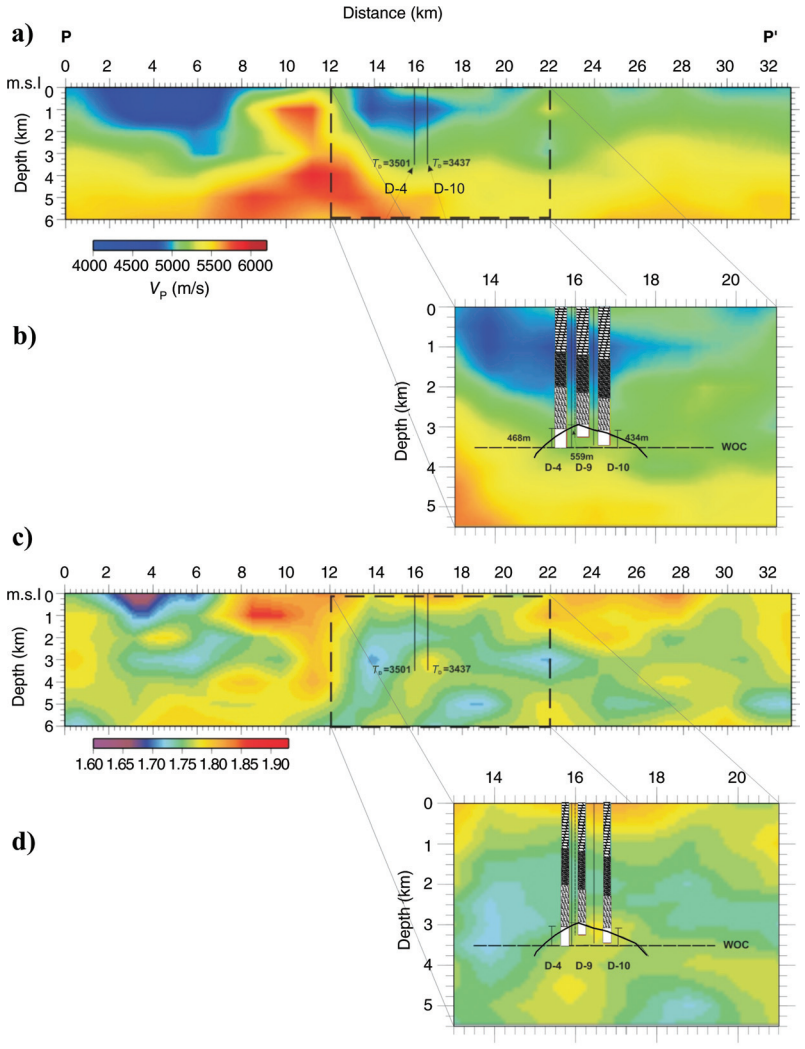

Figure 20. (a) V_P cross sections along line PP′. (b) Comparison with wells D-4 and D-10. (c) V_P/V_S cross sections along line PP′. (d) Comparison with wells D-4 and D-10. Dashed line labeled WOC is the water-oil contact.

ID: thangabaluP Time: 13:33 I Path: Q:/3b2/GPY#/Vol00000/110059/APPFile/AI-GPY#110059

J_ID: GPY DOI: 10.1190/1.3560016 Date: 10-March-11 Stage: Page: 17 Total Pages: 24

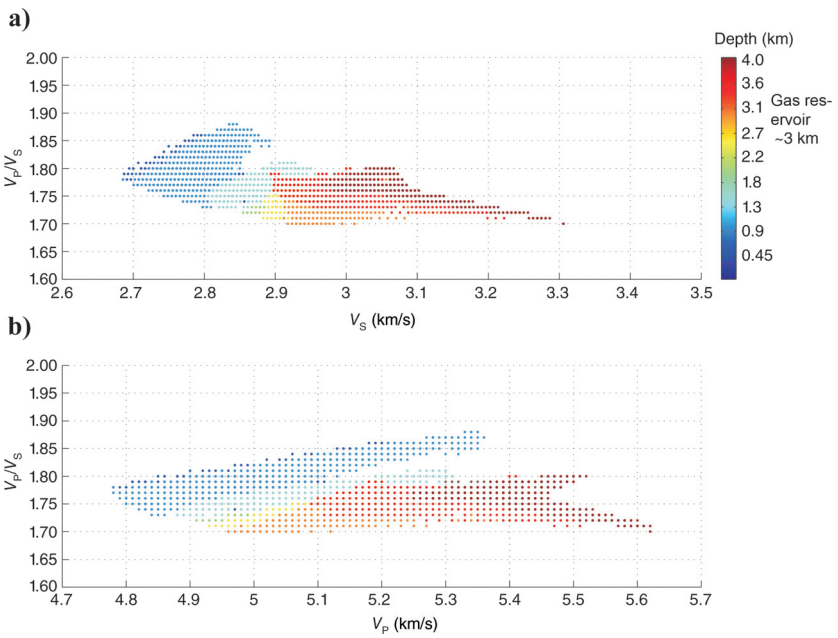

Figure 21. Relation between V_P/V_S and (a) V_S and (b) V_P for the gas-producing area at various depths.

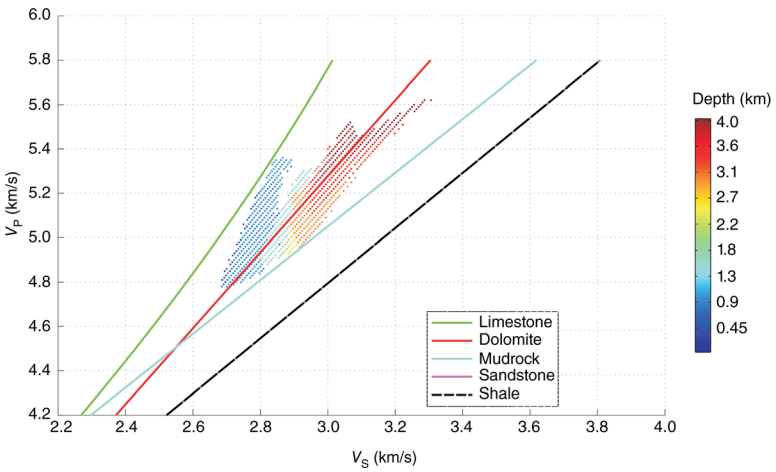

Figure 22. Relation between V_P and V_S versus depth for the gas-producing area. Mudrock-line data are from Castagna et al. (1985); all other data are from Castagna et al. (1993).

ID: thangabaluP Time: 13:35 I Path: Q:/3b2/GPY#/Vol00000/110059/APPFile/AI-GPY#110059

J_ID: GPY DOI: 10.1190/1.3560016 Date: 10-March-11 Stage: Page: 18 Total Pages: 24

distances between neighboring neurons are small, then these neurons represent a cluster of patterns with similar characteristics. If the neurons are far apart, then they are located in a zone of the input space that has few patterns and can be seen as a separation between clusters. The U-matrix constitutes a particularly useful tool to analyze the results of an SOM because it allows an appropriate interpretation of the clusters available in the data.

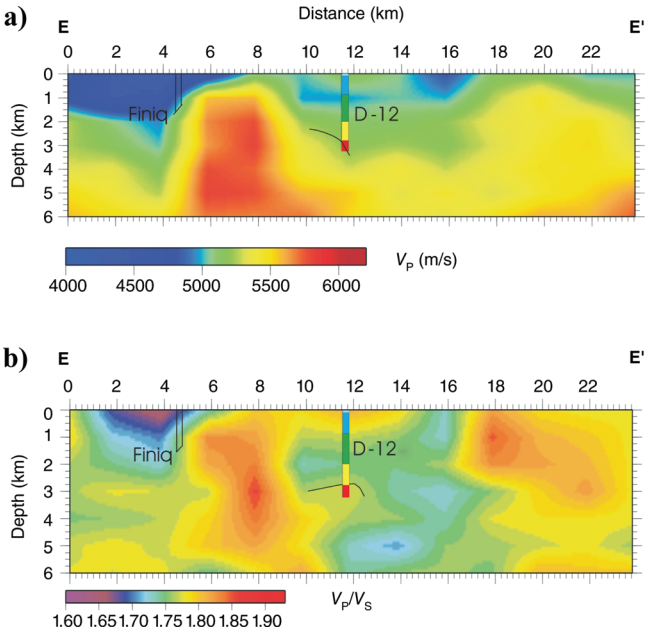

Figure 23. (a) V_P and (b) V_P/V_S cross sections passing through the Finiq oil field and well D-12.

SOM application and results

We applied the above methodology over a selected volume of the study area that included the oil and gas reservoirs. We trained the neural network by using V_P, V_S, Poisson's ratio ν, and Q_P 3D data (Figure 28). Because only two of these parameters are required to get the third, one might think that training the SOM with two of them is adequate. Klose (2003) proves that the results are further improved if we use all four parameters.

The initial step is to read all of the component parameters of the data and to construct the component planes for each of them as well

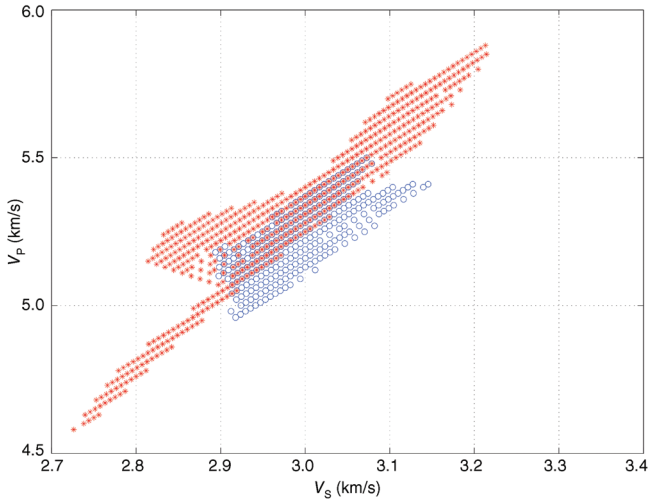

Figure 25. Relation between V_P and V_S, at the producing depths of the gas (blue circles) and oil (red stars) fields.

Figure 24. Relation between V_P/V_S and (a) V_S and (b) V_P for the oil-producing area at various depths.

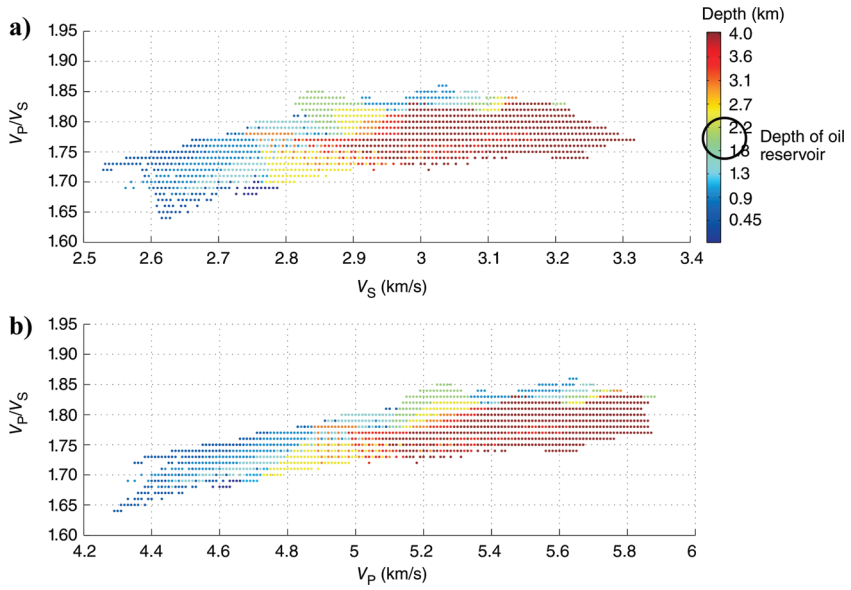

ID: thangabaluP Time: 13:35 I Path: Q:/3b2/GPY#/Vol00000/110059/APPFile/AI-GPY#110059

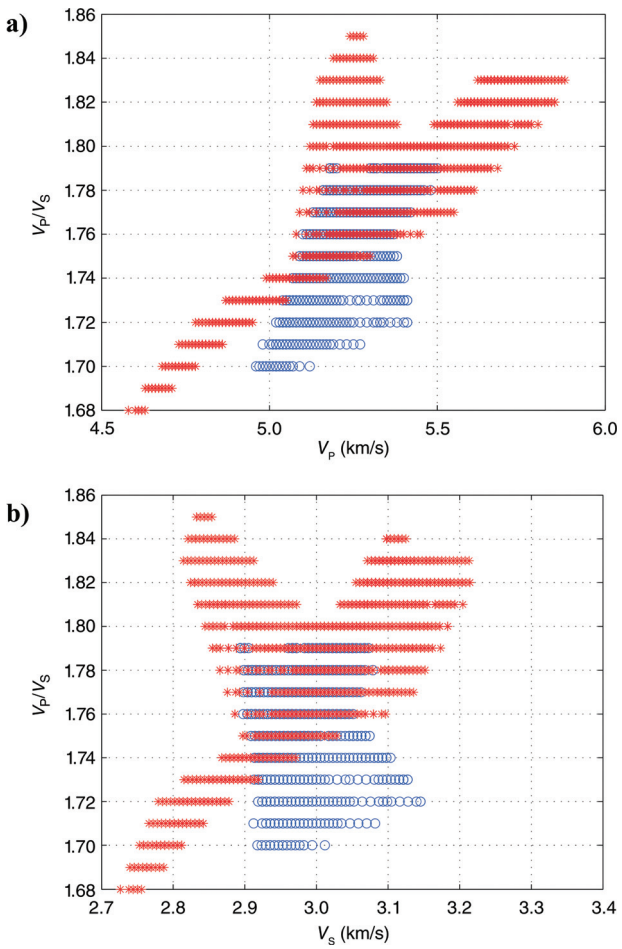

Figure 26. Relation between V_P/V_S and (a) V_P and (b) V_S at the producing depths of the gas (blue circles) and oil (red stars) fields.

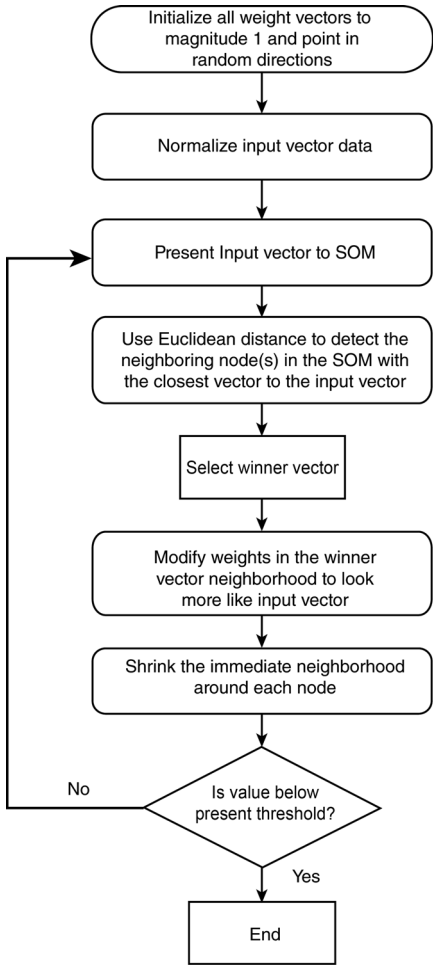

Figure 27. SOM network training process.

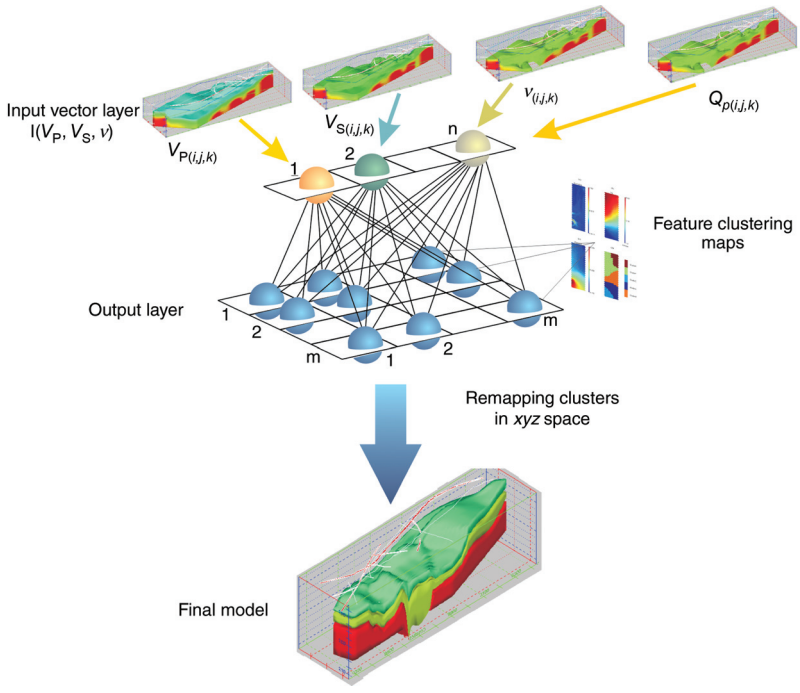

Figure 28. All input values of V_P, V_S, Poisson's ratio v, and Q_P data are used to train the neural network.

J_ID: GPY DOI: 10.1190/1.3560016 Date: 10-March-11 Stage: Page: 20 Total Pages: 24

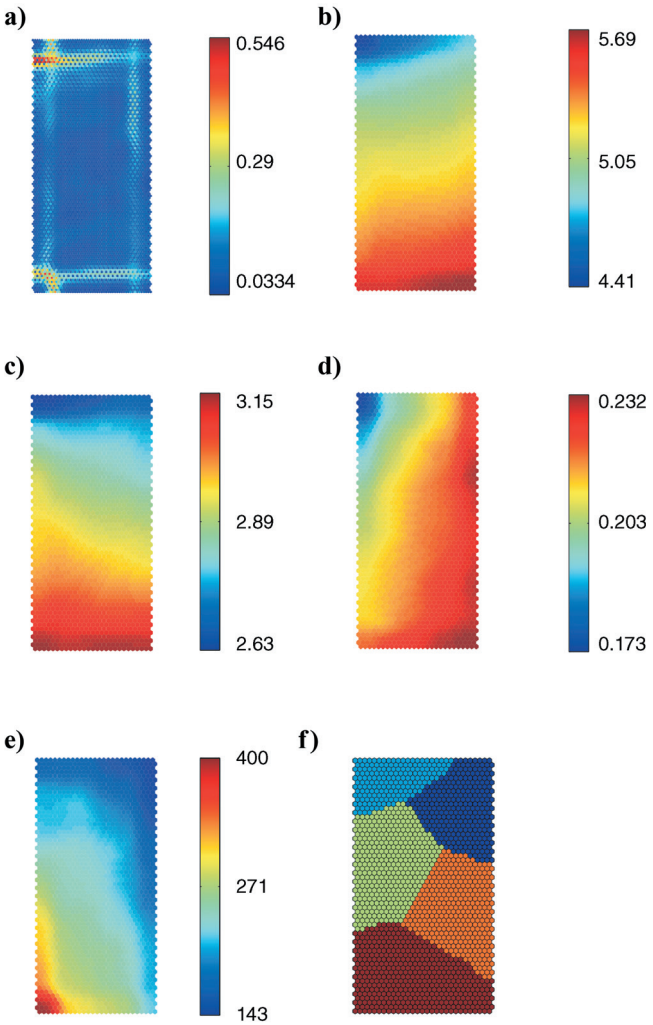

Figure 29. (a) U-matrix and the component planes, (b) V_P, (c) V_S, (d) Poisson's ratio v, (e) Q_P, and (f) the selected clusters.

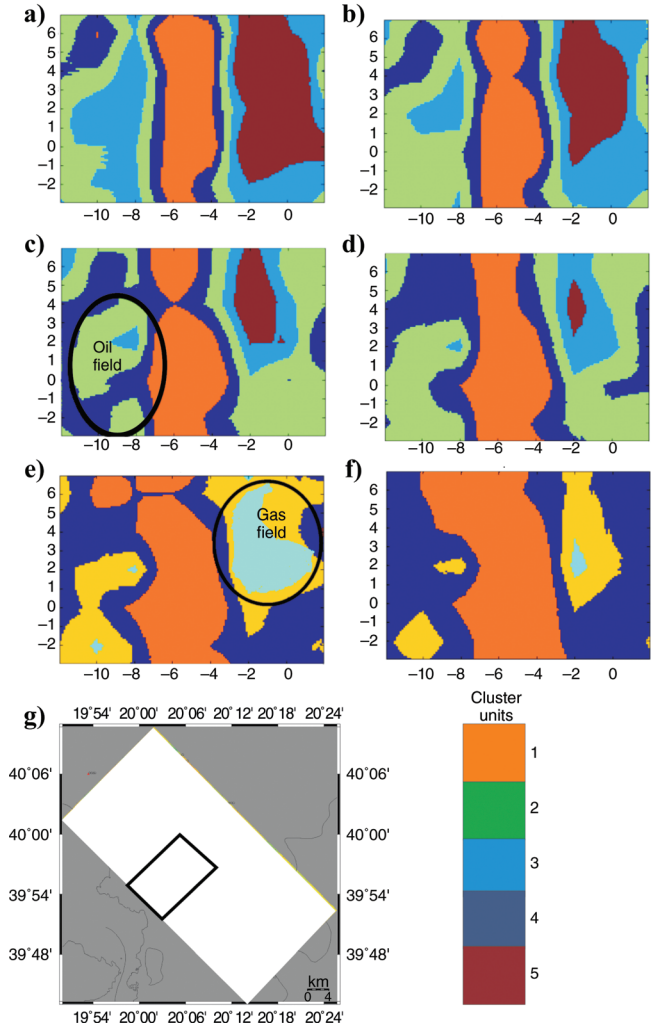

Figure 30. SOM clustering results presented as horizontal sections at depths of (a) 1, (b) 1.5, (c) 2, (d) 2.5, (e) 3, and (f) 3.5 km. Numerals measure the local grid coordinates (in kilometers). (g) The map indicates the location of the presented results on the tomography block. The color scale indicates the cluster as determined in Figure 29.

as to calculate the unified distance matrix (known as U-matrix) shown in Figure 29a–e. The next step is to define and separate the SOM data in clusters (Figure 29f). For this, the k-means clustering method is used. The Davies-Bouldin index (Davies and Bouldin, 1979) is calculated and used as a metric of the cluster separation. For us, calculating this index for an increasing number of clusters indicates that our data are best divided into five clusters.

Judging from Figure 29, we can see that the highest Poisson values for these seismic lines do not coincide with the lowest P-wave velocities, but they correlate with the lowest S-wave velocities of the medium. Also, the lowest Poisson values correlate better with higher V_S values than the V_P ones.

The results from the classification process are mapped in the form of horizontal sections at a spacing of 500 m (Figure 30). This achieves an automatic initial separation of the major lithologic units.

CONCLUSIONS

A microearthquake network consisting of 50 three-component stations was installed in southern Albania to perform a PST investigation of a hydrocarbon field. In the tomographic approach, traveltimes were used to estimate the P- and S-wave velocities, to infer variations of V_P/VS, and to construct various tomographic images. Furthermore, the 3D distribution of Q_P was inferred from first-pulse-width measurements. The results obtained were used to train a Kohonen neural network, and a lithological classification was attempted using data-clustering methods. The passive results showed a satisfactory correlation with the geologic features and the production characteristics of the existing wells in the area, and they explained the lateral distribution of the oil and gas reservoirs.

Based on comparisons between conventional seismic and PST data, it is obvious that PST can provide a wealth of information for this particular area where conventional 2D seismic surveys did not work well. PST is the most appropriate method for surveying

ID: thangabaluP Time: 13:38 I Path: Q:/3b2/GPY#/Vol00000/110059/APPFile/AI-GPY#110059

J_ID: GPY DOI: 10.1190/1.3560016 Date: 10-March-11 Stage: Page: 21 Total Pages: 24

this region because of the very complicated overthrust geotectonic regime, along with the presence of evaporitic structures.

ACKNOWLEDGMENTS

We thank Sven Treitel for his extremely useful comments and support, and we also thank Eleni Karagiorgi for her valuable comments on our paper. The comments of three reviewers were also taken into consideration and considerably improved this paper. LandTech Enterprises and Stream Oil are acknowledged for providing permission to publish the results of this investigation. Finally, we would like to thank the technical and scientific personnel of LandTech Enterprises, without whose contribution and professionalism this survey would not have been a success.

APPENDIX A

QUALITY CONTROL

The final step of the inversion procedure is to assess the resolution and reliability of the results. One metric most commonly used is the derivative weighted sum (DWS). The DWS provides a reliable estimate of the sampling of the investigated area by summing up all of the ray segments in the region of influence of one velocity parameter and weighting them according to the ray-velocity--parameter (node) distance.

The DWS is calculated (Toomey and Foulger, 1989) by

$$\mathrm{DWS}(a_n) = N \sum_i \sum_j \left(\int_{P_{ij}} \omega_n(x)\, ds \right), \tag{A-1}$$

where i and j are the event and station indices, ω_n is the weight used in the linear interpolation that depends on coordinate position, P_{ij} is the raypath between i and j, N is a normalization factor that takes into account the volume influenced by a_n, and ds is the segment along the raypath. The quantity DWS quantifies the relative ray density in the volume-of-influence of a model node, weighting the importance of each ray segment by its distance to the model node. It yields a rough estimate of the illumination of the model space. The DWS values depend on the ray-segment length.

The most appropriate method of estimating the reliability of the tomography results is by performing a synthetic sensitivity test. This procedure can provide information on the effects of the model grid spacing and the data distribution. Also, it can estimate the proximity of the calculated model parameters to the initial absolute values.

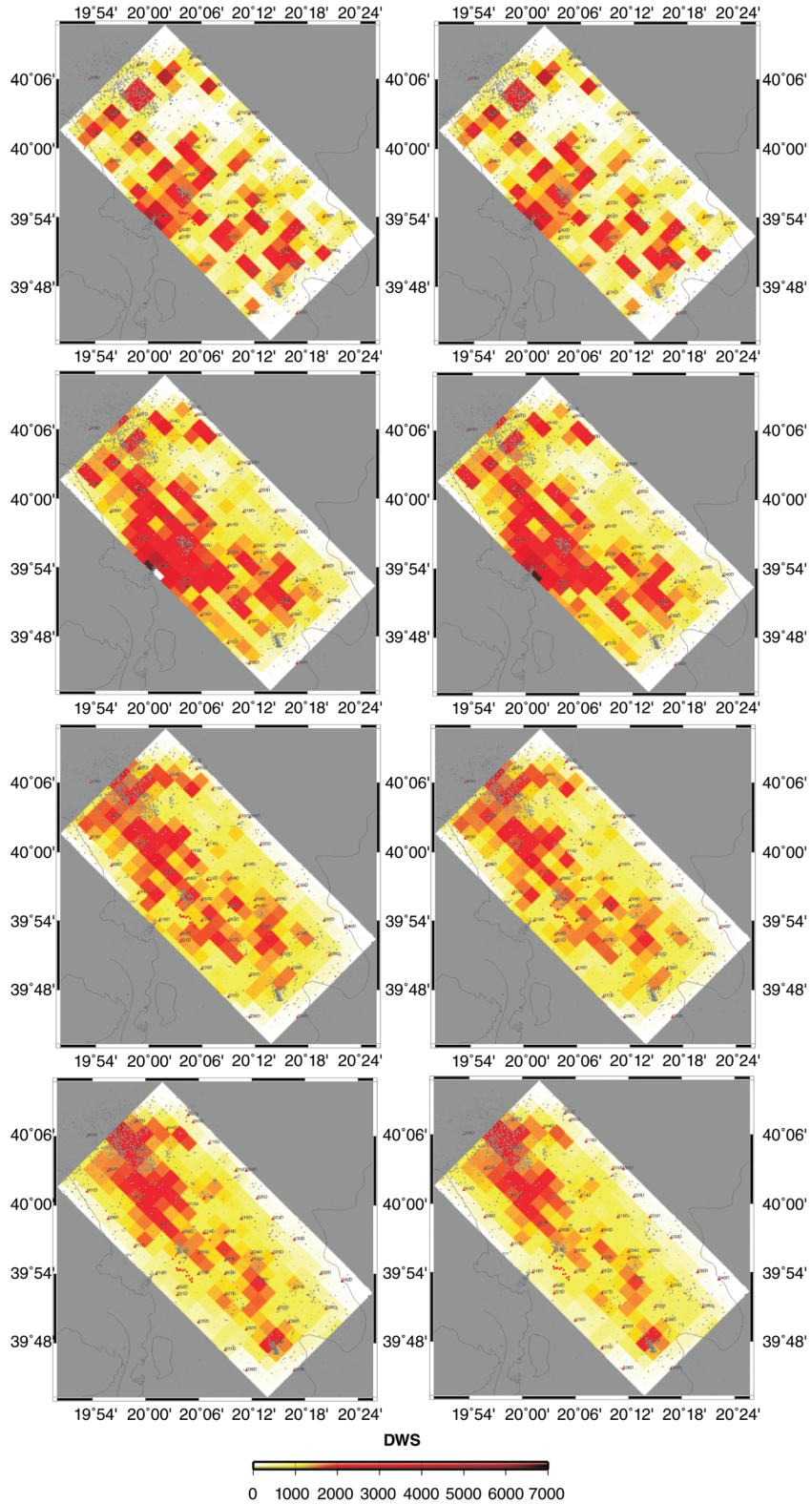

Figure A-1. DWS of V_P and V_P/V_S at 1-km spacing, ranging from 0 km on the top row to 3 km on the bottom row.

ID: thangabaluP Time: 13:39 I Path: Q:/3b2/GPY#/Vol00000/110059/APPFile/AI-GPY#110059

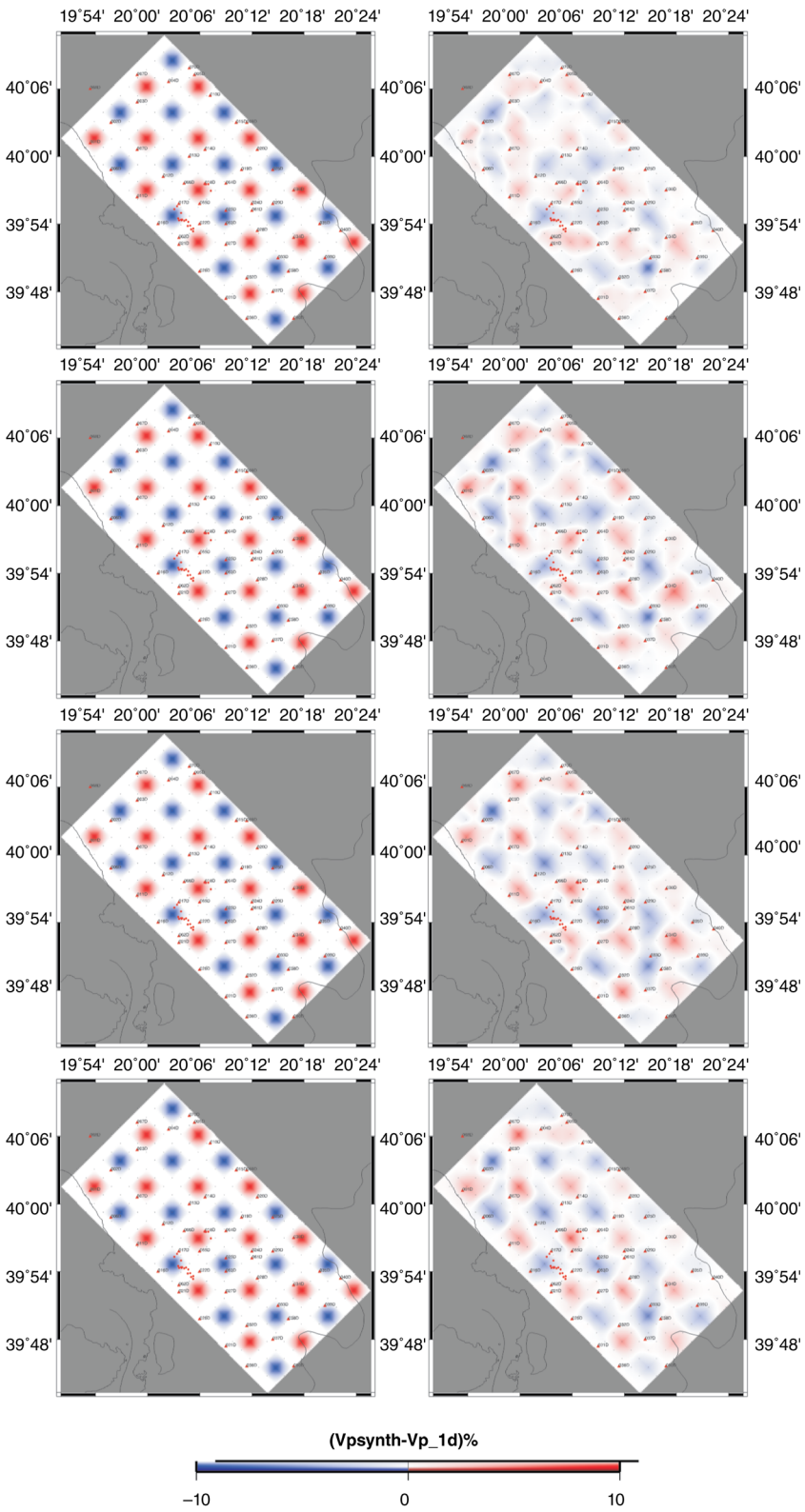

Figure A-2. Results of V_P checkerboard test at 1-km spacing, ranging from 0 km on the top row to 3 km on the bottom row. Left-hand-side views are the synthetic model; right-hand-side views are the inverted model.

In most cases, the checkerboard test is used, following the technique described for the feasibility study. Combining the above-mentioned methods can be very useful in identifying possible artifacts and consequently avoiding misinterpretations.

The DWS maps related to this investigation are presented in Figure A-1. The obtained V_P and V_P/V_S model is more accurate in areas with DWS values exceeding 500.

Next, synthetic checkerboards were generated by taking the 1D initial starting velocity models and superimposing a $\pm 10\%$ velocity perturbation (Figure A-2), applied in $2 \times 2 \times 1$-km model cells. Each transition from high to low velocity occurred over two model blocks because the regularization used in the inversion impeded the reconstruction of sharp velocity contrasts between model blocks.

Although the optimal horizontal wavelength in the checkerboard test is 1 km, structures with much shorter wavelength can be resolved by the data, e.g., the corners of the checkerboards are well imaged in the best-resolved regions. Synthetic traveltimes were calculated using the hypocenter-stations' geometry of the real data as well as the velocity distribution of the checkerboard model. Finally, Gaussian noise of zero mean and a standard deviation of 0.05 s was added to the resulting synthetic traveltimes. In the reconstructions, the original 1D velocity models were used as starting models, with the earthquake origin times and hypocenter locations randomly redistributed with zero-mean Gaussian noise and with a 0.1-s and 1-km standard deviation, respectively.

REFERENCES

Aubouin, J., 1959, Contribution a l'étude géologique de la Gréce septentrional: les confins de l'épire et de la Thessalie: Annales géologique des pays hélléniques, **10**, 1–525.

Aubouin, J., R. Blanchet, J.-P. Cadet, P. Celet, J. Charvet, J. Chorowicz, M. Cousin, and J.-P. Rampoux, 1970, Essai sur la geologie des Dinarides: Bulletin de la Société Géologique de France, **12**, 1060–1095.

Bacao, F., V. Lobo, and M. Painho, 2005, The self-organizing map, the Geo-SOM, and relevant variants for geosciences: Computers & Geosciences, **31**, no. 2, 155–163, doi:10.1016/j.cageo.2004.06.013.

Blair, D. P., and A. T. Spathis, 1982, Attenuation of explosion generated pulse in rock masses: Journal of Geophysical Research, **87**, no. B5, 3885–3892, doi:10.1029/JB087iB05p03885.

Bourbie, T., O. Coussy, and B. Zinszner, 1987, Acoustics of porous media: Butterworth-Heinemann Publishers.

Castagna, J. P., M. L. Batzle, and R. L. Eastwood, 1985, Relationships between compressional-wave and shear-wave velocities in clastic silicate rocks: Geophysics, **50**, 571–581, doi:10.1190/1.1441933.

Castagna, J. P., M. Batzle, and T. K. Kan, 1993, Rock physics — The link between rock properties and AVO response, *in* J. P. Castagna and M. M. Backus, eds., Offset-dependent reflectivity — Theory and practice of AVO analysis: SEG, 135–171.

Chang, H.-C., D. Kopaska-Merkel, and H.-C. Chen, 2002, Identification of lithofacies using Kohonen self-organizing maps: Computers & Geosciences, **28**, no. 2, 223–229, doi:10.1016/S0098-3004(01)00067-X.

Chiarabba, C., and A. Amato, 2003, V_p and V_p /V_s images in the M_w 6.0 Colfiorito fault region (central Italy): A contribution to the understanding of seismotectonic and seismogenic processes: Journal of Geophysical Research B: Solid Earth, **108**, no. B5, 2248–2265, doi:10.1029/2001JB001665.

Clawson, S. R., R. B. Smith, and H. M. Benz, 1989, P-wave attenuation of the Yellowstone caldera from three-dimensional inversion of spectral decay using explosion source seismic data: Journal of Geophysical Research, **94**, no. B6, 7205–7222, doi:10.1029/JB094iB06p07205.

Davies, D. L., and W. Bouldin, 1979, A cluster separation measure: IEEE Transactions on Pattern Analysis and Machine Intelligence, **1**, no. 2, 224–227, doi:10.1109/TPAMI.1979.4766909.

de Lorenzo, S., G. Di Grazia, E. Giampiccolo, S. Gresta, H. Langer, G. Tusa, and A. Ursino, 2004, Source and Q_P parameters from pulse width inversion of microearthquake data in southeastern Sicily, Italy: Journal of Geophysical Research, **109**, no. B7, B07308, doi:10.1029/2003JB002577.

de Lorenzo, S., M. Filippucci, E. Giampiccolo, and D. Patane, 2006, Intrinsic Qp at Mt. Etna from the inversion of rise times of 2002 microearthquake sequence: Annals of Geophysics, **49**, 1215–1234.

Durham, L. S., 2003, Passive seismic. Listen: Is it the next big thing?: AAPG Explorer, **24**, no. 4, 127–131.

Dvorkin, J., and A. Nur, 1996, Elasticity of high porosity sandstones: Theory for two North Sea data sets: Geophysics, **61**, 1363–1370, doi:10.1190/1.1444059.

Eberhart-Phillips, D., and A. J. Michael, 1998, Seismotectonics of the Loma Prieta, California, region determined from three-dimensional Vp, Vp/Vs, and seismicity: Journal of Geophysical Research B: Solid Earth, **103**, no. B9, 21099–21120, doi:10.1029/98JB01984.

Evans, J. R., D. Eberhart-Phillips, and C. H. Thurber, 1994, User's manual for SIMULPS12 for imaging Vp and Vp/Vs: A derivative of the Thurber tomographic inversion SIMUL3 for local earthquakes and explosions: U.S. Geological Survey Open-File Report 94–431.

Evans, J. R., and J. J. Zucca, 1988, Active high-resolution seismic tomography of compressional wave velocity and attenuation structure at Medicine Lace volcano, northern California Cascade Range: Journal of Geophysical Research, **93**, no. B12, 15016–15036, doi:10.1029/JB093iB12p15016.

Gladwin, M. T., and F. D. Stacey, 1974, Anelastic degradation of acoustic pulses in rock: Physics of the Earth and Planetary Interiors, **8**, no. 4, 332–336, doi:10.1016/0031-9201(74)90041-7.

Hamada, G. M., 2004, Reservoir fluids identification using Vp/Vs ratio?: Oil & Gas Science and Technology, **59**, no. 6, 649–654, doi:10.2516/ogst:2004046.

Haslinger, F., 1998, Velocity structure, seismicity and seismotectonics of northwestern Greece between the Gulf of Arta and Zakynthos: Ph.D. dissertation, Swiss Federal Institute of Technology.

Hedlin, K., L. Mewhort, and G. Margrave, 2001, Delineation of steam flood using seismic attenuation: 71st Annual International Meeting, SEG, Expanded Abstracts, 1592–1595.

Hoxha, V., 2001, The main geological features and prospects in Kercisht-Sorocol region (Korrab, eastern Albania): Ph.D. dissertation, University of Tirana.

ISPGJ-IGJN, 1982, Geology of Albania: ISPGJ-IGJN (Albanian Institute of Geological Research).

ISPGJ-IGJN, 1983, Geological map of Albania: ISPGJ-IGJN (Albanian Institute of Geological Research), scale 1:200,000.

Iyer, H. M., and K. Hirahara, 1993, Seismic tomography: Theory and practice: Chapman and Hall.

Kapotas, S., G.-A. Tselentis, and N. Martakis, 2003, Case study in NW Greece of passive seismic tomography: A new tool for hydrocarbon exploration: First Break, **21**, 37–42.

King, G. C. P., G.-A. Tselentis, J. Gomberg, P. Molnar, S. W. Roecker, H. Sinvhal, C. Soufleris, and J. M. Stock, 1983, Microearthquake seismicity and active tectonics of northwestern Greece: Earth and Planetary Science Letters, **66**, 279–288, doi:10.1016/0012-821X(83)90141-3.

Kissling, E., 1988, Geotomography with local earthquake data: Reviews of Geophysics, **26**, no. 4, 659–698, doi:10.1029/RG026i004p00659.

Kissling, E., W. L. Ellsworth, D. Eberhart-Phillips, and U. Kradolfer, 1994, Initial reference models in local earthquake tomography: Journal of Geophysical Research, **99**, no. B10, 19635–19646, doi:10.1029/93JB03138.

Kjartansson, E., 1979, Constant Q-wave propagation and attenuation: Journal of Geophysical Research, **84**, no. B9, 4737–4748, doi:10.1029/JB084iB09p04737.

Klose, C. D., 2003, Engineering geological rock mass characterization of granitic gneisses based on seismic in-situ measurements: Ph.D. dissertation, Swiss Federal Institute of Technology.

Kohonen, T., 1995, Self-organizing maps: Springer.

Kumar, G., M. Batzle, and R. Hofmann, 2003, Effect of fluids on attenuation of elastic waves: 73rd Annual International Meeting, SEG, Expanded Abstracts, 1592–1595.

Lee, W. H., and S. W. Stewart, 1981, Principles and applications of microearthquake networks: Advances in geophysics, supplement 2: Academic Press.

Liu, H. P., 1988, Effects of source spectrum on seismic attenuation measurements using the pulse broadening method: Geophysics, **53**, 1520–1526, doi:10.1190/1.1442433.

Liu, H. P., J. Warrick, B. Westerlund, and E. Kayen, 1994, In situ measurement of seismic shear wave absorption in the San Francisco Holocene Bay mud by the pulse-broadening method: Bulletin of the Seismological Society of America, **84**, 62–75.

Luan, N., V. Tari-Kovacic, and A. Putnikovic, 2002, Stratigraphy and evolution of Ionian foreland basin: Exploration methods in highly explored basins: 3rd International Symposium on Petroleum Geology, Croatian Academy of Sciences and Arts, Abstracts, 79–83.

Martakis, N., S. Kapotas, and G.-A. Tselentis, 2006, Integrated passive seismic acquisition and methodology: Case studies: Geophysical Prospecting, **54**, no. 6, 829–847, doi:10.1111/j.1365-2478.2006.00584.x.

Martakis, N., A. Tselentis, and S. Kapetas, 2003., Passive seismic tomography a complementary geophysical method: Successful case study: 65th Conference & Exhibition, EAGE, Extended Abstracts, P065.

Maxwell, S. C., and T. I. Urbancic, 2001, The role of passive microseismic monitoring in the instrumented oil field: The Leading Edge, **20**, 636–639, doi:10.1190/1.1439012.

Penn, B. S., 2005, Using self-organizing maps to visualize high-dimensional data: Computers & Geosciences, **31**, no. 5, 531–544, doi:10.1016/j.cageo.2004.10.009.

Pride, S. R., J. Harris, D. L. Johnson, A. Mateeva, K. T. Nihei, R. L. Nowack, J. Rector, H. Spetzler, R. Wu, T. Yamomoto, J. Berryman, and M. Fehler, 2003, Acquisition/processing — Permeability dependence of seismic amplitudes: The Leading Edge, **22**, no. 6, 518–525, doi:10.1190/1.1587671.

Ripley, B. D., 1996, Pattern recognition and neural networks: Cambridge University Press.

Robertson, A., and M. Shallo, 2000, Mesozoic-Tertiary tectonic evolution of Albania in its regional eastern Mediterranean context: Tectonophysics, **316**, no. 3–4, 197–254, doi:10.1016/S0040-1951(99)00262-0.

Rutledge, J. T., and W. S. Phillips, 2003, Hydraulic stimulation of natural fractures as revealed by induced microearthquakes, Carthage Cotton Valley gas field, East Texas: Geophysics, **68**, 441–452, doi:10.1190/1.1567212.

Rutledge, J. T., W. S. Phillips, and B. K. Schuessler, 1998, Reservoir characterization using oil-production-induced microseismicity, Clinton County, Kentucky: Tectonophysics, **289**, no. 1–3, 129–152, doi:10.1016/S0040-1951(97)00312-0.

Stacey, F. D., M. T. Gladwin, B. McKavanagh, A. T. Linde, and L. M. Hastie, 1975, Anelastic damping of acoustic and seismic pulses: Surveys in Geophysics, **2**, no. 2, 133–151, doi:10.1007/BF01447906.

Thurber, C. H., 1983, Earthquake locations and three-dimensional crustal structure in the Coyote Lake area, central California: Journal of Geophysical Research, **88**, no. B10, 8226–8236, doi:10.1029/JB088iB10p08226.

——, 1986, Analysis methods for kinematic data from local earthquakes: Reviews of Geophysics, **24**, no. 4, 793–805, doi:10.1029/RG024i004p00793.

Thurber, C. H., S. R. Atre, and D. Eberhart-Phillips, 1995, Three-dimensional Vp and Vp/Vs structure at Loma Prieta, California, from local earthquake tomography: Geophysical Research Letters, **22**, no. 22, 3079–3082, doi:10.1029/95GL03077.

Toomey, D. R., and G. R. Foulger, 1989, Tomographic inversion of local earthquakes data from the Hengill-Grendsalur central volcano complex, Iceland: Journal of Geophysical Research, **94**, no. B12, 17497–17510, doi:10.1029/JB094iB12p17497.

Tselentis, G., 1998, Intrinsic and scattering seismic attenuation in W. Greece: Pure and Applied Geophysics, **153**, no. 2–4, 703–712, doi:10.1007/s000240050215.

Tselentis, G., P. Paraskevopoulos, and N. Martakis, 2010, Intrinsic Q_p seismic attenuation from the rise time of microearthquakes: A local scale application at Rio-Antirrio, western Greece: Geophysical Prospecting, **58**, no. 5, 845–859, doi:10.1111/j.1365-2478.2010.00885.x.

Tselentis, G., E. Sokos, N. Martakis, and A. Serpetsidaki, 2006, Seismicity and seismotectonics in Epirus, western Greece: Results from a microearthquake survey: Bulletin of the Seismological Society of America, **96**, no. 5, 1706–1717, doi:10.1785/0120020086.

Um, J., and C. H. Thurber, 1987, A fast algorithm for two-point seismic ray tracing: Bulletin of the Seismological Society of America, **77**, 972–986.

Underhill, J. R., 1989, Late Cenozoic deformation of the Hellenide foreland, western Greece: Geological Society of America Bulletin, **101**, 613–634.

Valoroso, L., L. Improta, P. De Gori, R. Di Stefano, L. Chiaraluc, and C. Chiarabba, 2008, From 3D to 4D passive seismic tomography — The

sub-surface structure imaging of the Val d Agri region, S. Italy: 70th Annual EAGE Conference & Exhibition, Extended Abstracts, P028.

Vanorio, T., J. Virieux, P. Capuano, and G. Russo, 2005, Three-dimensional seismic tomography from *P* wave and *S* wave microearthquake travel times and rock physics characterization of the Campi Flegrei caldera: Journal of Geophysical Research, **110**, no. B3, B03201, doi:10.1029/2004JB003102.

Velaj, T., 2001, Evaporites in Albania and their impact on the thrusting process: Journal of the Balkan Geophysical Society, **4**, no. 1, 9–18.

Vesanto, J., E. Alhoniemi, J. Himberg, K. Kiviluoto, and J. Parviainen, 1999, Self-organizing map for data mining in MATLAB: The SOM toolbox: Simulation News Europe, **25**, 54.

Villmann, T., R. Der, M. Herrmann, and T. M. Martinetz, 1997, Topology preservation in self-organizing feature maps: Exact definition and measurement: IEEE Transactions on Neural Networks, **8**, no. 2, 256–266, doi:10.1109/72.557663.

Virieux, J., 1991, Fast and accurate ray tracing by Hamiltonian perturbation: Journal of Geophysical Research, **96**, no. B1, 579–594, doi:10.1029/90JB02025.

Winkler, K. W., and A. Nur, 1979, Pore fluids and seismic attenuation in rocks: Geophysical Research Letters, **6**, no. 1, 1–4, doi:10.1029/GL006i001p00001.

——, 1982, Seismic attenuation: Effects of pore fluids and frictional-sliding: Geophysics, **47**, no. 1, 1–15, doi:10.1190/1.1441276.

Wu, H., and J.Lees, 1996, Attenuation structure of Coso geothermal area, California, from wave pulse widths: Bulletin of the Seismological Society of America, **86**, 1574–1590.

Zhang, H., S. Sarkar, M. N. Toksöz, H. S. Kuleli, and F. Al-Kindy, 2009, Passive seismic tomography using induced seismicity at a petroleum field in Oman: Geophysics, **74**, no. 6, WCB57–WCB69, doi:10.1190/1.3253059.

Zollo, A., and S. de Lorenzo, 2001, Source parameters and three-dimensional attenuation structure from the inversion of microearthquake pulse width data: Method and synthetic tests: Journal of Geophysical Research, **106**, no. B8, 16287–16306, doi:10.1029/2000JB900463.

Zucca, J. J., L. J. Hutchings, and P. W. Kasameyer, 1994, Seismic velocity and attenuation structure of the Geysers geothermal field, California: Geothermics, **23**, no. 2, 111–126, doi:10.1016/0375-6505(94)90033-7.